1 **Impact of scale-aware deep convection on the cloud liquid and ice water paths and precipitation using the**

2 **Model for Prediction Across Scales (MPAS-v5.2)**

3 Laura D. Fowler[1], Mary C. Barth[1], and Kiran Alapaty[2]
4 [1]National Center for Atmospheric Research, Boulder, Colorado
5 [2]Center for Environmental Measurements and Modeling, U.S. Environmental Protection Agency
6 Research Triangle Park, North Carolina

8
9
10 May 2020
11
12
13
14
15
16
17
18
19
20
21
22
23
24
25
26
27
28
29
30
31
32
33
34
35
36
37
38
39
40
41
42
43
44
45
46
47
48

49 *Corresponding author address*: Dr. Laura D. Fowler, National Center for Atmospheric Research. P.O. Box 3000,

50 Boulder, CO 80307-3000, USA.

51 E-mail: laura@ucar.edu

Abstract. The cloud Liquid Water Path (LWP), Ice Water Path (IWP), and precipitation simulated with uniform- and variable-resolution numerical experiments using the Model for Prediction Across Scales (MPAS) are compared against Clouds and the Earth's Radiant Energy System (CERES) and Tropical Rainfall Measuring Mission data. Our comparison between monthly mean model diagnostics and satellite data focuses on the convective activity regions of the Tropical Pacific Ocean, extending from the Eastern Tropical Pacific Basin where trade wind boundary layer clouds develop to the Western Pacific warm pool characterized by deep convective updrafts capped with extended upper-tropospheric ice clouds. Using the scale-aware Grell-Freitas (GF) and Multi-Scale Kain-Fritsch (MSKF) convection schemes in conjunction with the Thompson cloud microphysics, uniform-resolution experiments produce large biases between simulated and satellite-retrieved LWP, IWP, and precipitation. Differences in the treatment of shallow convection lead the LWP to be strongly overestimated when using GF while being in relatively good agreement when using MSKF compared to CERES data. Over areas of deep convection, uniform- and variable-resolution experiments overestimate the IWP with both MSKF and GF, leading to strong biases in the top-of-the-atmosphere long- and short-wave radiation relative to satellite-retrieved data. Mesh refinement over the Western Pacific warm pool does not lead to significant improvement in the LWP, IWP, and precipitation due to increased grid-scale condensation and upward vertical motions. Results underscore the importance of evaluating clouds, their optical properties, and the top-of-the-atmosphere radiation budget in addition to precipitation when performing mesh refinement global simulations.

1   Introduction

Comparing simulated against observed global cloud liquid and ice water paths (LWP and IWP) remains challenging because of uncertainties in parameterizing moist processes and cloudiness in global climate and numerical weather prediction (NWP) models, and errors in retrieving the LWP and IWP from satellite measurements. Cloud simulations from general circulation models (GCMs) involved in Phase 3 and 5 of the Coupled Model Intercomparison Project (CMIP3; CMIP5; Meehl et al, 2007; Taylor et al., 2012) display a strong disparity in the simulated LWP (Jiang et al., 2012; Li et al., 2018) and IWP (Li et al., 2012), producing annual mean LWP and IWP overestimated by factors of 2 to 10 compared to satellite data. Satellite observations of the LWP and IWP from passive nadir viewing instruments such as the Moderate-resolution Imaging Spectroradiometer (MODIS; Minnis et al., 2011), and profiling radar such as the 94-GHz instrument on the CloudSat satellite (Stephens et al., 2002), also display major differences among themselves, as discussed in Li et al. (2008) and Waliser et al. (2009). While models and satellite retrievals agree that the LWP and IWP should be defined as the vertically-integrated liquid and ice water content, including all nonprecipitating and precipitating hydrometeors, this is not always the case in practice, further challenging a clearly-posed data-data and model-data comparison. Defining the LWP and IWP varies between models, depending on the complexity of the parameterization of cloud microphysics processes and prognostic versus diagnostic treatment of falling hydrometeors. Defining the measured LWP and IWP varies between satellite products, depending on the sensitivity of the observing systems to detect large precipitating particles. While comparing simulated and observed LWP and IWP may not be as straightforward as comparing the top-of-the-atmosphere (TOA) radiation budget (Dolinar et al., 2015; Stanfield et al., 2015), it offers a different way to directly diagnose biases in simulated total cloud liquid

87 and ice water mass as a first step to help correct deficiencies in parameterizing global scale moist processes and

88 precipitation.

89 Before the launch of the CloudSat and Cloud-Aerosol Lidar and Infrared Pathfinder Satellite Observation mission

90 (Stephens et al., 2002), global estimates of the LWP and IWP were retrieved principally from satellite radiance

91 measurements over different spectral intervals (e.g., Alishouse et al., 1990; Greenwald et al., 1993; Minnis et al., 1995;

92 Platnick et al., 2003). In their critical review of most common methods developed to retrieve cloud and precipitation

93 properties from satellite radiances, Stephens and Kummerow (2007) identify two main sources of errors. The first

94 source of errors originates from the mandatory classification between cloudy and cloud-free scenes, and between

95 precipitating and non-precipitating cloudy scenes. The second source of errors stems from using forward radiative

96 transfer models that lack details of the vertical distribution of cloudiness and precipitation as well as complexity in

97 specifying the optical properties of liquid water and ice particles. Estimating the LWP and IWP from CloudSat radar

98 reflectivity alone presents its own set of challenges for scenes that include precipitating cloud systems due to the high

99 sensitivity of radar reflectivity to the presence of large particles, for scenes that include mixed-phase and deep

100 convective clouds, and close to the surface due to ground clutter. Li et al. (2018) show that annual mean maps of

101 MODIS- and CloudSat-based LWP agree relatively well in tropical and subtropical regions if both data sets exclude

102 LWP observations for deep convective/precipitating clouds since MODIS is quite insensitive to precipitation.

103 Stephens and Kummerow (2007) advocate combining satellite-retrieved radar and radiance measurements to help

104 validate simulated cloud properties and precipitation. In addition to considering the impact of precipitating particles,

105 Waliser et al. (2009) demonstrate that a well-posed model-data comparison must include a consistent sampling

106 between model outputs and satellite data to reduce diurnal sampling biases and sensitivity of the sensor and retrieval

107 algorithm to the particle size when computing the simulated LWP and IWP.

108 Contemporary climate and NWP GCMs (Giorgetta et al., 2018; Molod et al., 2012; Kay et al., 2015, Skamarock

109 et al., 2012) categorize moist processes into three distinct parameterizations, one to simulate turbulent mixing in the

110 Planetary Boundary Layer (PBL) in response to surface forcing and forcing in the free troposphere, one to simulate

111 subgrid scale shallow and deep convection, and one to include grid-scale cloud microphysics. While coupling between

112 parameterizations varies between GCMs, it is an established practice to let detrained condensates from convective

113 updrafts serve as sources for non-convective grid-scale clouds, as precipitating anvils and cirrus outflow. We suggest

114 that uncertainties in parameterizing moist convection and impact on grid-scale clouds may explain a major part of the

115 differences in the LWP and IWP simulated between the CMIP3 and CMIP5 GCMs. In recent years, efforts have been

116 made to develop unified cloud parameterizations to represent all cloud types and alleviate the need to parameterize

117 complex interactions between stratiform, shallow convective, and deep convective clouds (Guo et al., 2015; Storer et

118 al., 2015; Thayer et al., 2015). Using the global Model for Prediction Across Scales (MPAS; Skamarock et al., 2012),

119 Fowler et al. (2016) discuss the sensitivity of simulated precipitation as spatial resolution increases from hydrostatic

120 to nonhydrostatic scales and suggest to further analyze the associated sensitivity of simulated clouds and TOA

121 radiation. Results show that as subgrid scale convective motions are increasingly resolved, diagnostic precipitation

122 from the scale-aware Grell-Freitas (GF; Grell and Freitas, 2014) deep convection scheme decreases while prognostic

123 precipitation from the WSM6 (Hong and Lim, 2006) cloud microphysics scheme increases over the refined area of

124 the variable-resolution mesh. Vertical profiles of the cloud liquid and ice water mixing ratios and cloud fraction
125 highlight the redistribution of cloud condensates and relative humidity with height in the refined area in response to
126 decreased contribution of convective detrainment of cloud liquid water and ice. However, Fowler et al. (2016) do not
127 further address if variations in the vertical profiles of cloud condensates lead to improved LWP, IWP, and cloud optical
128 properties against satellite-derived data.

129 The objectives of our research are threefold. First, we want to assert that our suite of PBL, deep and shallow
130 convection, and cloud microphysics parameterizations tested in MPAS at hydrostatic and nonhydrostatic scales for
131 medium-range spring forecasts over the Continental United States (Schwartz, 2019; Wong and Skamarock, 2016) can
132 also be used to produce month-long simulations of tropical convection, narrowing our analysis on the Tropical Pacific
133 Ocean. In order to broaden our research and possibly generalize our results, we also implemented the scale-aware
134 MultiScale Kain-Fritsch (MSKF; Glotfelty et al., 2019; Zheng et al., 2016) parameterization of deep and shallow
135 convection in addition to GF. Second, we want to evaluate the ability of MPAS to simulate the LWP, IWP, cloudiness,
136 and TOA long- and short-wave radiation against the Clouds and the Earth's Radiant Energy System (CERES; Wielicki
137 et al., 1996) Single Scanner FootPrint (SSF; Minnis et al., 2011) data set, and precipitation against the TRMM
138 Multisatellite Precipitation Analysis (TMPA; Huffman et al., 2007). Our third goal aims at understanding differences
139 in the LWP, IWP, precipitation, and cloud radiative effects as functions of horizontal resolution with GF and MSKF
140 using the capability of local mesh refinement developed for MPAS.

141 In Section 2, we summarize the characteristics of the GF and MSKF parameterizations of deep and shallow
142 convection. In Section 3, we provide a short description of MPAS, including physics parameterizations used with both
143 convective parameterizations, the design of our experiments using the uniform- and variable-resolution meshes, and
144 description of the satellite data sets used to validate our results. In Section 4, we analyze our results in terms of
145 precipitation and varying contribution of the convective and grid-scale precipitation to the total precipitation as a
146 function of horizontal resolution. In Section 5, we compare the LWP, IWP, and TOA long- and short-wave radiation
147 against satellite data. In Section 6, we discuss some of our findings. Finally, in Section 7, we summarize our results
148 and propose areas of future research.

149 **2   Description of the convective parameterizations**

150 Mass flux-based convective parameterizations distinguish themselves through the use of different triggering
151 functions to initiate convection, the details of their entraining-detraining cloud models, and formulation of their
152 closures that control the intensity of convection and computation of the cloud base mass flux. For convective
153 parameterizations that include deep and shallow convection, criteria that characterize the two kinds of convection
154 strongly vary. Furthermore, how convective parameterizations account for the dependence of convection on the
155 horizontal resolution differs in complexity. In this section, we summarize the chief characteristics of GF and MSKF,
156 including differences in their treatment of deep and shallow convection, and horizontal-scale dependence.

2.1 The Grell-Freitas (GF) parameterization

The version of GF used in our numerical experiments is that implemented in version 3.8.1 of the Advanced Research Weather Research Forecast model (Skamarock et al., 2008), as described in Grell and Freitas (2014). Its properties are first discussed in Grell (1993) and later expanded in Grell and Devenyi (2002) to include stochasticism. GF treats deep and shallow convection separately by using different initial entrainment rates (7×10^{-5} m^{-1} and 1×10^{-2} m^{-1} for deep and shallow convection, respectively) to control the depth of convective layers and different closures to calculate the cloud base mass flux. GF includes an ensemble of closures from well-known convective parameterizations to compute a mean cloud-base mass flux. For deep convection, these four closures are the *AS* closure (Arakawa and Schubert, 1974) that assumes instantaneous equilibrium between the large-scale forcing and subgrid-scale convection; the *W* closure (Brown, 1979; Frank and Cohen, 1987) that relates the cloud base mass flux to the grid-scale upward vertical velocity; the *MC* closure (Krishnamurti et al., 1983) that calculates the cloud base mass flux as a function of the vertically-integrated vertical moisture advection; and the *KF* closure (Kain and Fritsch, 1993) that reduces the convective available potential energy over a prescribed convective time-scale. Qiao and Liang (2015) analyze the separate and combined impacts of the four closures on the simulated summer precipitation over the United States coastal oceans. On the one hand, they found that computing the cloud base mass flux using the *W* and *MC* closures led to precipitation patterns and amounts that are in better agreement against TMPA data than those using the *AS* and *KF* closures. On the other hand, they found that the *AS* and *KF* closures yield improved diurnal cycle of precipitation relative to the other two closures. In our numerical experiments, GF gives an equal weight to each closure to calculate the mean cloud base mass flux for deep convection. As for deep convection, GF includes different closures for shallow convection. In our numerical experiments using GF, we choose the boundary layer quasi-equilibrium (*BLQE*) closure of Raymond (1995) for shallow convection.

Both types of convection transport total water and moist static energy in a conservative manner but neglect to include ice phase processes in updrafts and downdrafts. In this version of GF, the only feedback between shallow convection and the large-scale environment is lateral and cloud-top detrainment of water vapor and corresponding heating, as liquid water formed in shallow updrafts evaporates immediately. Deep convection returns potential temperature, water vapor, and condensed water tendencies to the environment. Detrained condensed water acts as a source of liquid water (ice) if the large-scale temperature is warmer (colder) than the prescribed 258 K threshold. While GF assumes that shallow convective plumes are not deep enough to produce precipitation, the conversion of liquid water to rain water in deep convective plumes depends on a simple Kessler-type (Kessler, 1969) conversion threshold and precipitation reaches the surface instantaneously.

As discussed in Grell and Freitas (2014), deep convection includes a simplified representation of the unified parameterization of deep convection described in Arakawa and Wu (2013). Arakawa and Wu (2013) demonstrate that mass flux-based convective parameterizations can be modified to work at all resolutions spanning between hydrostatic and nonhydrostatic scales through the reduction of the convective vertical eddy transport as a quadratic function of the horizontal fraction of the grid box occupied by convective updrafts. In GF, the convective updraft fraction (σ) is

192   computed as a simple function of the initial entrainment rate ($\varepsilon = 7\text{x}10^{-5}$ m^{-1}) and half-width radius (R) of convective

193   updrafts following Simpson and Wiggert (1969), or

194    $$\sigma = \frac{\pi R^2}{A} \quad \text{and} \quad R = \frac{0.2}{\varepsilon} \tag{1}$$

195   where A is the area of the grid box. In Eq. (1), σ is not allowed to exceed 0.7, based on the discussion of Grell and

196   Freitas (2014). As discussed in Fowler et al. (2016), when σ becomes greater than 0.7, σ is set to 0.7 and ε is

197   recalculated using Eq. (1), leading to increased entrainment and decreased convective cloud-tops as A becomes

198   smaller. Another option would be to turn off deep convection when σ reaches values close to 1, in which case a better

199   choice for its maximum value may be between 0.9 and 1 (Grell and Freitas, 2014). Figure 1.a highlights the rapid

200   decrease in σ from 0.7 to 0.3 as spatial resolution decreases from 6 to 9 km. σ further decreases from 0.3 to 0.1 for

201   resolutions between 9 and 16 km, and from 0.1 to 0.05 for resolutions between 16 and 30 km. The $(1-\sigma)^2$ quadratic

202   function used to scale the mass flux starts to be significant at resolutions greater than 20 km and decreases rapidly to

203   a minimum value of 0.1 for horizontal grid-spacing smaller than 6 km. Using a maximum value for σ ensures that

204   over the most refined area of the mesh, parameterized deep convection is not completely turned off since deep

205   convection is not explicitly resolved. Using a variable-resolution mesh varying between 50 km over the coarse area

206   of the mesh down to 3 km over the refined area of the mesh centered over South America, Fowler et al. (2016) show

207   that the impact of parameterized deep convection weakens and that of grid-scale cloud microphysics strengthens as

208   horizontal grid-spacing increases from hydrostatic to nonhydrostatic scales.
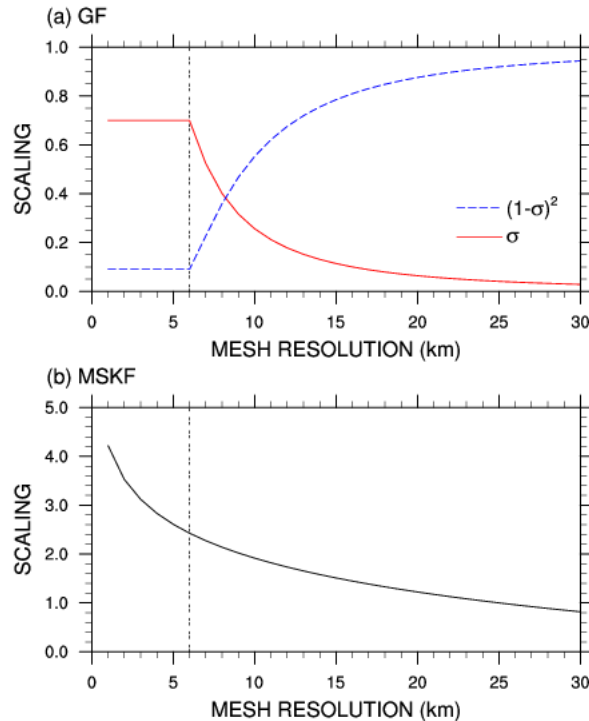
209
210   **Figure 1: (**a) Convective updraft fraction as a function of the mesh resolution used to scale the cloud base mass flux in GF; and (b)
211   scaling factor as a function of the mesh resolution used to scale the convective time-scale in MSKF.

2.2   The Multi-Scale Kain-Fritsch (MSKF) parameterization

MSKF is the scale-aware version of the Kain-Fritsch (KF) convective parameterization, first developed by Kain and Fritsch (1990; 1993), and later updated by Kain (2004) to include, among other improvements, non-precipitating shallow convection. The trigger function is that used in Fritsch and Chappell (1980), originally tested in Kain and Fritsch (1992) and recently in Suhas and Zhang (2014). In MSKF, convection may be triggered if the temperature of a *mixed layer* is greater than that of the environment. The pressure thickness of that mixed layer must be at least 50 hPa thick and is computed as the sum of adjacent layer depths starting at the layer next to the surface. The mixed layer temperature is a pressure-weighted function of the temperatures in those adjacent layers after being lifted to the Lifting Condensation Level (LCL) plus a perturbation temperature linked to the magnitude of the grid-scale vertical motion at the LCL. Once the base of a potential updraft source layer is found, convection remains activated if the vertical velocity of an air parcel lifted using the Lagrangian parcel method remains positive for a minimum cloud depth of 3 km, as a test that the convective instability is strong enough for the air parcel to reach the Level of Free Convection (LFC). If not, the procedure is repeated by moving up to the next model layer until a new updraft source layer is found or until the search reaches above the lowest 300 hPa of the atmosphere. Further details on the equations used to compute the perturbation temperature and parcel vertical velocity are found in Kain (2004).

In MSKF, the closure assumption assumes that the Convective Available Potential Energy in a cloud layer is removed within a time adjustment period following Bechtold et al. (2001). The convective time-scale is defined as the advective time-scale in the cloud layer with maximum values of 1 h and 0.5 h for deep and shallow convection, respectively. In contrast to GF, the thermodynamics inside the cloud model includes the ice phase. The condensed water formed in each cloudy layer is partitioned between liquid water and ice, assuming a linear transition of the cloud temperature between 268 K and 248 K. A fraction of the condensed water converts to rain, following Ogura and Cho (1973), and reaches the ground instantaneously. As discussed in Kain (2004), when an updraft source layer is identified, the classification of a convective cloud layer as deep or shallow depends on the cloud depth. Shallow convection is activated when all the criteria for deep convection are met, but the depth of the updraft is shallower than the minimum cloud depth (3 km). This definition implies that shallow and deep convection are not allowed to coexist. In the case of shallow convection, precipitation formed in updrafts is detrained to the environment as rain or snow, providing an additional moisture source to the large-scale environment. As in GF, MSKF provides tendencies of temperature, water vapor, cloud liquid water/ice to the environment, and tendencies of rain and snow from shallow convection.

MSKF contains many improvements over KF, as summarized in the supplemental material of Glotfelty et al. (2019). These improvements include subgrid-scale cloud feedbacks to radiation from both shallow and deep convection leading to more realistic surface downward radiation, as described in Alapaty et al. (2012), and the scale dependence of fundamental parameters so that MSKF can be used at spatial resolutions varying between hydrostatic and nonhydrostatic scales. As detailed in Glotfelty et al. (2019) and Zheng et al. (2016), MSKF uses a scale dependent formulation (β) to the adjustment time-scale (τ) for deep and shallow convection based on Bechtold et al. (2008), or

$$\tau = \frac{H}{W_{cl}}\,\beta \quad \text{and} \quad \beta = 1 + ln\left(\frac{25}{\Delta x}\right) \tag{2}$$

248 where H and W_{cl} are the depth of the convective cloud and cloud-averaged vertical velocity scale, and Δx is the grid

249 spacing. Figure 1.b highlights the dependence of the β scaling parameter as a function of horizontal resolution. As

250 many MSKF parameters are optimized for a resolution around 25 km (Kain, 2004), β is equal to 1 at 25 km, ramping

251 up to values greater than 2.4 for resolutions higher than 6km. Because the adjustment time-scale is proportional to

252 β (Zheng et al., 2016), it increases as horizontal resolution increases, leading to scale-aware stabilization of the

253 atmosphere by MSKF. In addition, MSKF includes a new scale-aware formulation of the minimum entrainment rate

254 using the LCL as a function of the scale-dependent *Tokioka* parameter (Tokioka et al., 1988), a scale-dependent

255 conversion rate for liquid water and ice condensates to precipitation, an increased grid-scale velocity expressed in

256 terms of the subgrid scale updraft mass flux, and elimination of double counting of precipitation in cloudy layers. The

257 separate and combined impacts of the development of MSKF on high resolution weather forecasts and regional climate

258 simulations are discussed in Herwehe et al. (2014), Mahoney (2016), He and Alapaty (2018), Zheng et al. (2016), and

259 Glotfelty et al. (2019).

260 ## 3   Methodology

261 ### 3.1   Numerical experiments

262   We discuss differences in our MPAS results between GF and MSKF configurations on precipitation, cloud

263 properties, and TOA radiation using 30-day long numerical experiments in MPAS (Skamarock et al., 2012). MPAS

264 is a global nonhydrostatic atmospheric model developed for NWP and climate studies. The horizontal discretization

265 uses an unstructured spherical centroidal Voronoi tessellation with a C-grid staggering, as described in Ju et al. (2011),

266 while the vertical discretization is the height-based hybrid terrain-following coordinate of Klemp (2011). The

267 dynamical solver integrates the prognostic equations (cast in flux form) for the horizontal momentum, vertical

268 velocity, potential temperature, dry air density, and scalars using the split-explicit technique of Klemp et al. (2007).

269 The temporal discretization uses a third-order Runge-Kutta scheme and the explicit time-splitting technique described

270 in Wicker and Skamarock (2002). We use the monotonic option of the scalar transport scheme of Skamarock and

271 Gassmann (2011) for horizontal and vertical advection of all moist scalars on the unstructured Voronoi mesh. Finally,

272 horizontal filtering of the state variables is based on Smagorinsky (1963), as described in Skamarock et al. (2012). For

273 variable-resolution meshes, the eddy viscosity coefficient is scaled as a function of the inverse mesh density so that

274 horizontal diffusion is increased in the coarse area relative to the refined area of the mesh.

275   In MPAS, the computational flow includes three distinct steps. The first step calls the physics parameterizations

276 that update the surface energy budget and calculate the tendencies of potential temperature, moist species, and zonal

277 and meridional wind due to long- and short-wave radiation, sub-grid scale convection, condensation and mixing in

278 the PBL and free troposphere, and gravity wave drag due to orography. The physics parameterizations use the same

279 input surface boundary conditions and soundings to compute their respective tendencies. Besides GF and MSKF, these

280 parameterizations are,

281 • the Noah land surface parameterization described by Chen and Dudhia (2001),

282   •   the long- and short-wave Rapid Radiative Transfer Model for GCMs (RRTMG) described by Mlawer et al. (1997)
283   and Iacono et al. (2000),
284   •   the semi-empirical parameterization of the cloud fraction of grid-scale clouds from Xu and Randall (1996) and
285   convective clouds from Xu and Krueger (1991) for use in the long- and short-wave RRTMG schemes. Following
286   Xu and Randall (1996), the fractional amount of grid-scale clouds is a function of the relative humidity and grid-
287   averaged condensate mixing ratio of cloud liquid water, ice, and snow. In MSKF, the fractional amount of shallow
288   and deep convective clouds depends on the convective mass flux.
289   •   the Mellor–Yamada–Nakanishi–Niino (MYNN) Planetary Boundary Layer (PBL) and surface layer scheme
290   described by Nakanishi and Niino (2009) with many updates described in Olson et al. (2019), and
291   •   the gravity wave-drag parameterization of Hong et al. (2008).

292   The second step calls the dynamical solver which updates the state variables with their respective diabatic
293 tendencies in conjunction to applying horizontal and vertical advection. Finally, the third step calls the grid-scale cloud
294 microphysics parameterization so that at the end of the model time-step, supersaturation has been entirely removed or
295 the relative humidity does not exceed 100%. Unlike the physics parameterizations listed in step one, the grid-scale
296 cloud microphysics scheme updates the potential temperature and moist species for the next time-step instead of
297 providing individual tendencies. The bulk cloud microphysics parameterization of Thompson et al. (THOM; 2004,
298 2008) is used in all our numerical experiments. THOM includes prognostic equations for temperature, mass mixing
299 ratio of water vapor, cloud liquid water, rain, cloud ice, snow, and graupel, and number concentration of cloud ice and
300 rain. We set the number concentration of cloud droplets to 300×10^6 m^{-3} over land and 100×10^6 m^{-3} over oceans. In
301 RRTMG, we diagnose the radiative effective radii of cloud liquid water, cloud ice, and snow as functions of the
302 THOM cloud particle assumptions to add coupling between the cloud microphysics and cloud optical properties, as
303 discussed in Thompson et al. (2016).

304   To compare the two convective parameterizations against satellite-derived data at hydrostatic scales, we use a
305 quasi-uniform resolution mesh for which the mean distance between cell centers is 30 km, corresponding to 655,362
306 cells. The vertical scale includes 55 layers with monotonically increasing thicknesses varying from 50 meters next to
307 the surface to 700 meters below 10 km to 1000 meters below the model top over ocean cells. The model top is set at
308 30 km. The dynamics and physics time-steps are both set to 150 s, and the horizontal diffusion length scale is set to
309 30 km. Long- and short-wave radiation is called every 15 mins and THOM is cycled twice so that the cloud
310 microphysics time-step is less than 90 s to ensure computational stability (Thompson, private communication). With
311 each convection scheme, we have performed a one-month long experiment preceded by a two-day spin-up to simulate
312 Northern Hemisphere early winter, initializing our experiments with ERA-Interim (Dee et al., 2011) reanalyses for
313 0000 UTC 29 November 2015. ERA-Interim sea surface temperatures and sea ice fractions are used to update ocean
314 cells daily. We refer to our quasi-uniform resolution experiments run with GF and MSKF as GFu and MSKFu,
315 respectively.

3.2 Sensitivity experiments

Using a variable-resolution mesh spanning between 50 km and 3 km in MPAS, Fowler et al. (2016) demonstrate that subgrid-scale convection parameterized with GF weakens and grid-scale cloud microphysics parameterized with WSM6 (Hong and Lim, 2006) strengthens as resolution increases from the coarse to the most refined area of the mesh. Over the most refined area, grid-scale precipitation contributes a major part to total precipitation, and vertical profiles of subgrid-scale deep convective heating and drying resemble those obtained with a precipitating shallow convection scheme. Fowler et al. (2016) suggest investigating the effect of variable resolution on cloud macrophysical properties and TOA radiation, as grid-scale cloud microphysics parameterizations provide a more physically-based description of condensation and precipitation over the refined area of the mesh, compared to simpler entraining-detraining cloud models used in parameterized convection schemes. With the aim to quantify changes in cloud properties and radiation across scales using GF and MSKF, we repeat the early winter experiments but with a variable-resolution mesh that spans between 30 km and 6 km and includes 1,622,018 cells. As shown in Fig. 2.a, we center the refined area of the mesh over the Pacific warm pool defined as the area of the Western Pacific Ocean where sea-surface temperatures (SSTs) exceed 28.5°C, or between 170°E and 140°W. East of 140°W, the north-south width of warmest SSTs across the transition zone between the refined and coarse mesh narrows to delineate the location of the ITCZ in the Tropical Eastern Pacific. West of 170°E, the end of mesh refinement borders the eastern tip of Papua New Guinea. Along the Equator, the transition zone between nonhydrostatic and hydrostatic scales spans 20° in the meridional direction on either side of the most refined area of the mesh.

INITIAL SEA-SURFACE TEMPERATURE (°C)
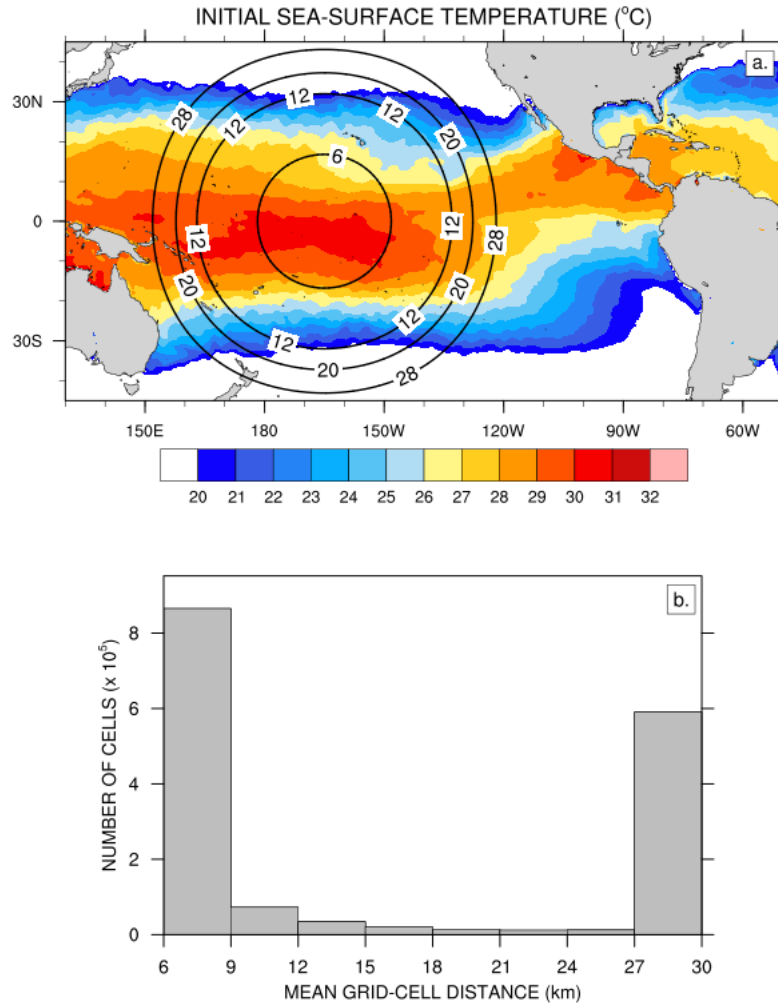
334
335 **Figure 2: (**a) Initial sea-surface temperature and refined variable-resolution mesh depicted using isolines of the mean distance
336 between grid-cell centers (km) over the Tropical Pacific Ocean; and (b) histogram of the number of cells as a function of the mean
337 distance between grid-cell centers.

338 Figure 2.b displays a histogram of the mean distance between grid-cell centers. Differences between the initialization

339 of the variable- and quasi uniform-resolution experiments include a reduced time-step from 150 s to 30 s and a reduced

340 minimum horizontal diffusion length scale from 30 km to 6 km. Also, THOM is called only once per physics time-

341 step. We refer to our variable-resolution experiments run with GF and MSKF as GFv and MSKFv, respectively.

342 Differences between GFu, GFv, MSKFu, and MSKFv are listed in Table 1. We acknowledge that running single 30-

343 day long experiments is a non-traditional way to assess the performance of convective parameterizations in an NWP

344 framework but is needed to provide increased satellite sampling when comparing simulated clouds and precipitation

345 against observations. Judt (2020) computes the predictability of the atmosphere using global convection-permitting

346 simulations with the same version of MPAS as in this study, but with a global uniform mesh with a 4 km cell spacing.

347 Results show that the predictability of the tropics (> 20 days) is longer than that of the extratropics and polar regions

348 (~ 2 weeks) when deep convection is mostly resolved. Using the Center for Ocean-Land-Atmosphere Studies GCM

349 with a triangular T63 truncation and the relaxed Arakawa-Schubert parameterization of deep convection (Moorthi and

350 Suarez, 1992), Strauss and Paolino (2008) demonstrate greater predictability in the tropics than in the extratropics at

351 hydrostatic scales. As our comparison between experiments and satellite data focuses on the tropical Pacific Ocean,
352 we are confident that biases arising during the first 2 weeks persist at longer time-scales and remain clearly depicted
353 in their monthly means. In order to further assess the robustness of our results, we also compare the 30-day versus 10-
354 day mean LWP, IWP, and precipitation to ensure that biases discussed in Sections 4 and 5 are qualitatively similar as
355 those observed at shorter time-scales (not shown for brevity).

	GFu	MSKFu	GFv	MSKFv
No. of cells	655,362	655,362	1,622,018	1,622,018
Min. cell distance (km)	22.8	22.8	4.4	4.4
Max. cell distance (km)	31.8	31.8	37.8	37.8
Time-step (s)	150	150	30	30
Minimum diffusion length scale (km)	30	30	6	6
CP	GF	MSKF	GF	MSKF

356 **Table 1:** Horizontal mesh resolution, minimum and maximum distance between grid-cell centers, time-step, horizontal diffusion
357 length scale, and convective parameterization (CP) for numerical experiments with the quasi uniform- and variable-resolution
358 meshes.

3.3   Satellite data sets

360   We compare the cloud liquid water path (LWP) and ice water path (IWP), cloud area fraction (CF), and the top-
361 of-the-atmosphere longwave upward (TOALW) and shortwave net (TOASW) radiation simulated in our numerical
362 experiments against the Edition-4 Single Scanner Footprint (SSF) products from the Clouds and the Earth's Radiant
363 Energy System (CERES; Wielicki et al., 1996). Minnis et al. (2011) describe in great details the retrieval of
364 simultaneous and collocated radiation fluxes and cloud properties from the CERES radiometers and the Moderate-
365 resolution Imaging Spectroradiometer (MODIS) using consistent algorithms and calibration across satellite platforms,
366 and shared auxiliary input (temperature and humidity profiles). SSF data are available in two different formats. The
367 first data file format contains one hour of radiation fluxes and cloud properties at the instantaneous CERES 20 km
368 footprint level from the sun-synchronous afternoon (morning) equatorial crossing time Aqua (Terra) satellites. As
369 illustrated in Minnis et al. (2011; their Fig. 15), the CF in each SSF is given in terms of a clear fraction, a fraction for
370 an upper and lower cloud layer separately, and a fraction for an upper layer over a lower layer, although the overlap
371 CF is not available and set to zero in the Edition 4 release version that we are using. The LWP, IWP, and all other
372 cloud fields are provided for the lower and upper layers, separately. Figure 3 illustrates two orbits of the Aqua satellite,
373 one between 00 GMT and 01 GMT, and one between 14 GMT and 15 GMT, showing the TOALW (top panel) and
374 CF (bottom panel), after gridding the hourly orbital data to a 0.2°x0.2° latitude-longitude grid. Gridded radiation fluxes
375 and cloud data are means over all SSF data contained inside each rectangular grid, after applying a linear interpolation
376 to reduce the number of missing values. Missing values, highlighted in gray in all figures, depict rectangular grids that
377 did not contain radiation and cloud data in any of the SSF inside the 0.2°x0.2° grid. As seen in Fig. 3, our gridding of
378 the orbital data removes most of the missing data along each orbit, providing a clear depiction of the relationship

379 between the TOALW and CF for cloudy and cloud-free grid cells. Areas of high (low) TOALW coincide with areas
380 of small (large) cloudy areas, but it is also interesting to note that areas of each orbit are characterized as overcast in
381 conjunction with areas that are not as spatially uniform in TOALW as in CF.
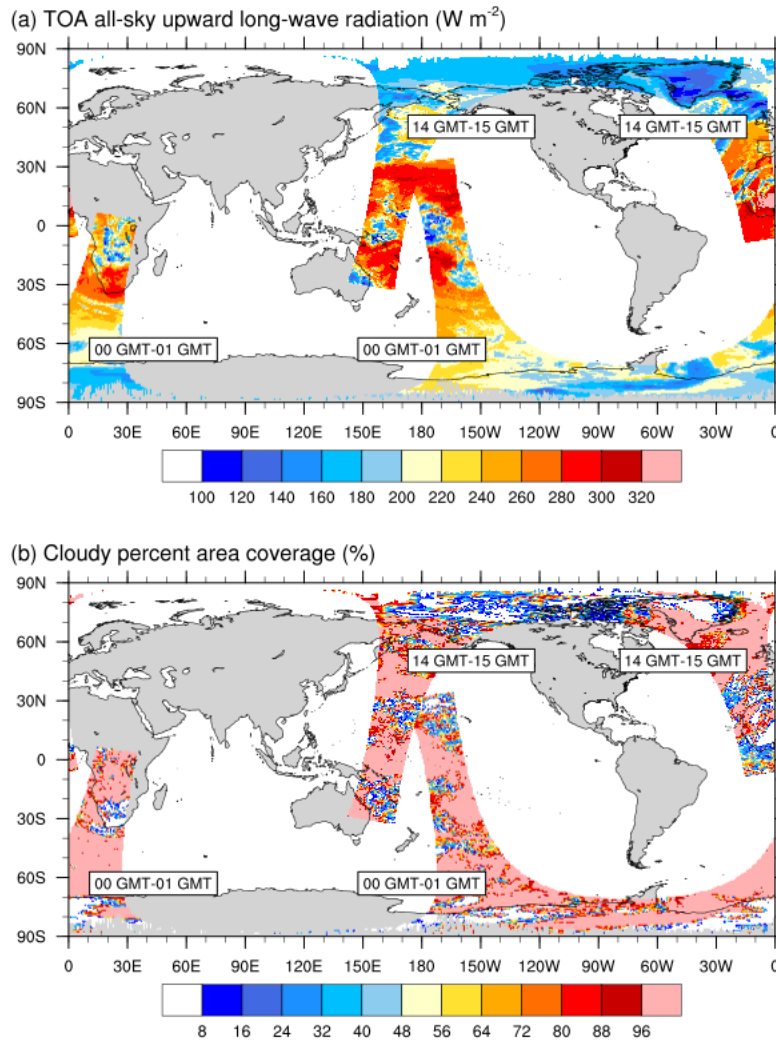
382
383 **Figure 3:** Orbital paths of the Aqua satellite between 00 GMT-01 GMT and 14 GMT-15 GMT after binning the SSF data onto a
384 0.2°x0.2° rectangular grid for (a) the TOA all-sky upward long-wave radiation, and (b) the cloudy percent area coverage for 1st
385 December 2015.

386   The second data file format (SSF1deg) includes daily and monthly averages of the original SSF orbital data but
387 interpolated on a 1°x1° latitude-longitude grid. The difficulty in using hourly higher-resolution orbital data instead of
388 monthly mean lower-resolution 1°x1° latitude-longitude gridded product is that the former are available in two distinct
389 *dynamic* layers while the latter is provided at fixed pressure levels and for the atmospheric column. The lower and
390 upper layers are referred to as *dynamic* layers because the cloud-top (base) pressure of each layer varies between SSFs
391 along each orbit. The advantage of using orbital hourly data is that they can be gridded and interpolated to a spatial
392 resolution close to that of our uniform and variable-resolution numerical experiments prior to computing monthly
393 mean radiation and cloud fields. We choose the 0.2°x0.2° latitude-longitude gridded hourly data derived from the first
394 data file format through the entire manuscript.

395   In order to best compare the simulated against satellite-derived LWP and IWP, we need to understand the
396   partitioning of the SSF LWP and IWP between the two cloud layers. In brief, a lower and an upper cloud layer can be
397   detected simultaneously if they lie adjacent to each other inside an SSF. In that case, the cloud properties for each
398   layer are reported separately. In the case when an opaque upper cloud layer is detected to be above a lower cloud
399   layer, it is impossible to identify the two layers separately. Then, only one cloud layer is reported and always classified
400   as the lower cloud layer, regardless of its cloud-base (top) pressure (Loeb, private communication). Further details on
401   the cloud classification, including determination of the cloud phase, are found in Geier et al. (2003) and Minnis et al.
402   (2011). Figure 4 shows the monthly-mean LWP, IWP, and CF for the lower (left panels) and upper (right panels) layer
403   measured by Aqua for December 2015 over the Tropical Pacific Ocean. Figure S1 is as Fig. 4, but for the Terra satellite
404   (see supplemental figures). LWP and IWP are *in-cloud* values meaning that they have not been weighted by CF. The
405   lower cloud layer includes stratiform clouds that form over colder sea-surface temperatures along the coast of Peru
406   and off the Baja Peninsula. Over these areas of CF greater than 72% for the lower cloudy layer, CF for the upper cloud
407   layer is less than 8%, highlighting that a single layer of low-level clouds fills a major fraction of the SSF. Increased
408   values of CF are seen in conjunction with increased (decreased) values for the LWP (IWP) in the lower cloud layer
409   indicative of warm-phase clouds, as well seen as off the coast of Peru. High values for the CF and IWP juxtaposed
410   with lower values for the LWP in the lower cloud layer depict clearly deep convection over the Eastern Pacific Ocean,
411   ITCZ, and warm pool region. Over areas of deep convection, upper cloud layers are often detected in conjunction with
412   lower cloud layers within the same SSF but are defined by decreased values for the CF and IWP. For the LWP, the
413   coexistence of a lower and upper cloud layer is quite infrequent, as seen by the number of missing grid-points in Fig.
414   4.b (S1.b). Where detected, the LWP in the upper layer exceeds that in the lower layer, indicative of warm-phase
415   mature thicker cumulus clouds coexisting with developing thinner cumulus clouds in the lower layer. Finally, outside
416   of the typical stratus cloud regions and either sides of the ITCZ and warm pool region, SSF data reveal extended
417   regions of warm-phase thinner clouds characteristic of widespread shallow convection over tropical oceans.
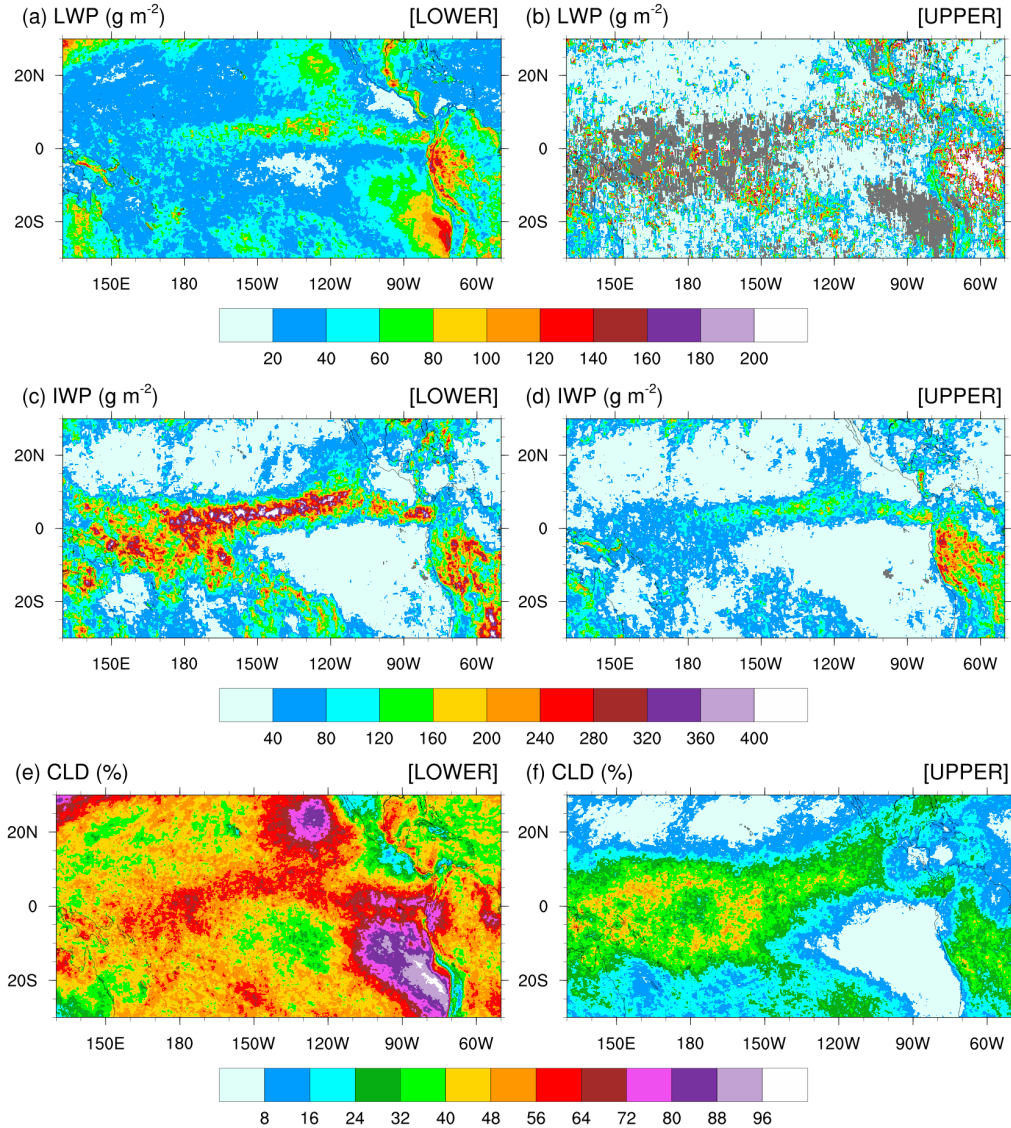
418
419 **Figure 4:** Monthly-mean cloud liquid water path (LWP, top panels), cloud ice water path (IWP, middle panels), and cloud fraction
420 (CLD, bottom panels) over the Tropical Pacific Ocean for December 2015 from the Aqua satellite. Panels (a), (c), and (e) are for
421 the lower cloud layer; panels (b), (d), and (f) are for the upper cloud layer.

422   Calculating the satellite-retrieved LWP and IWP in an atmospheric column for validation of those from our
423 numerical simulations is a two-step process. Because simulated LWPs and IWPs are *grid-cell mean* values and not
424 *local* values, we first multiply the SSF LWP and IWP by CF to get their mean values in the lower and upper cloud
425 layers separately, prior to gridding the hourly orbital data. Second, because the lower and upper layers are defined as
426 adjacent to each other and never overlap in an SSF, we simply add the grid-cell mean LWP and IWP in the lower layer
427 to that in the upper layer to compute the total LWP and IWP. Our processing method is simpler than the processing
428 steps taken by the CERES Science Team to spatially grid and temporally average SSF hourly orbital data to SSF1deg
429 gridded monthly mean data. Figure 5 compares the monthly-mean 0.2°x0.2° latitude-longitude CF-weighted LWP
430 and IWP and CF (left panels) against the SSF1deg products (right panels) for December 2015 over the Tropical Pacific
431 Ocean. The top panels of Fig. 5 show that our method reproduces successfully the geographical patterns and magnitude

432 of the LWP over the Tropical Pacific when compared against the SSF1deg data for both months. In contrast, because
433 our method does not weigh the IWP as a function of height, it systematically overestimates the SSF IWP when
434 compared against the SSF1deg data, as seen over the ITCZ and South Pacific Convergence Zone (SPCZ) in both
435 months.

436
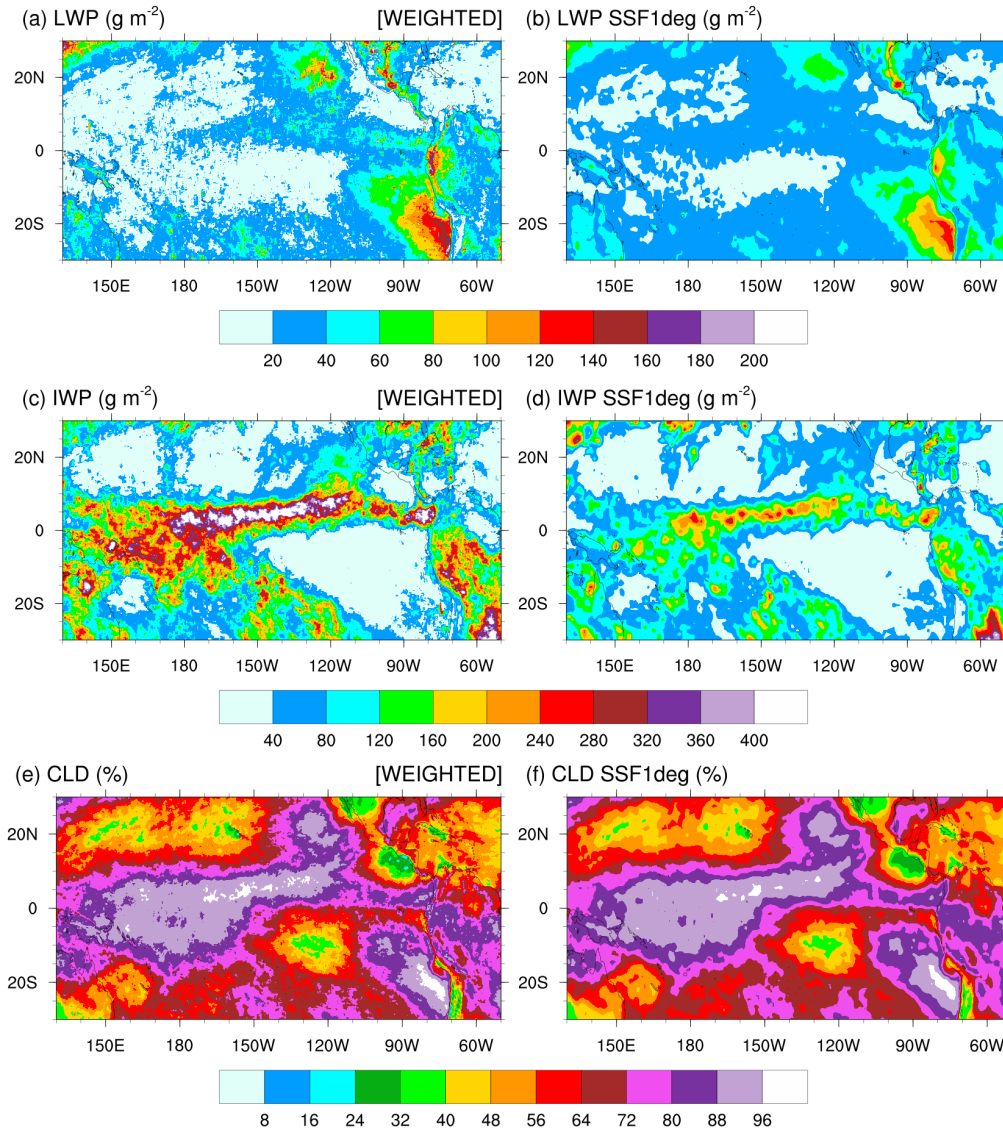
437
438 **Figure 5:** Monthly-mean cloudy area-weighted cloud liquid water path (LWP, top panels), cloudy-area weighted cloud ice water
439 path (IWP, middle panels), and cloud fraction (CLD, bottom panels) over the Tropical Pacific Ocean for December 2015. Panels
440 (a), (c), and (e) are SSF data; panels (b), d), and (f) are SSF1deg climatological data.

441   Using ice water content data from the ascending (daytime) and descending (nighttime) portion of CloudSat orbits,
442 Waliser et al. (2009; Fig. 7) estimate that day-night fluctuations in the ice water content at 215 hPa account for as
443 much as 13% (20 %) of the annual mean ice water content over the warm pool (Tropical Eastern Pacific), in response
444 to the diurnal cycle of deep convection over the tropical oceans. Therefore, when computing the monthly-mean CF,
445 LWP, IWP, TOALW, and TOASW produced with GFu, GFv, MSKFu and MSKFv, we first sample the hourly model

446 diagnostics in accordance with the Aqua and Terra satellite orbits in order to reduce biases from different diurnal
447 sampling between our experiments and SSF data. Because the MODIS-based retrieval of the LWP and IWP is
448 insensitive to precipitation, and the rain, snow, and graupel mixing ratios are prognostic variables in THOM and fall
449 through the atmosphere at finite velocities, we infer that the LWP and IWP must include all precipitating and non-
450 precipitating condensates.

451 In addition to CERES SSF data, we use the monthly-mean precipitation rates from the TRMM Multisatellite
452 Precipitation Analysis (TMPA Version 7; Huffman et al., 2007) to compare simulated versus observed precipitation
453 rates, and monthly mean ERA-Interim reanalyses (Dee et al., 2011) to compare simulated versus observed precipitable
454 water in the lower troposphere.

4 Simulated versus satellite-retrieved precipitation

4.1 Incidence of subgrid-scale shallow and deep convection

457 Differences in the treatment of interactions between shallow and deep convection in GF and MSKF, as described
458 in Section 2, are bound to modify the partitioning between shallow and deep convection as spatial resolution increases
459 over the refined area of the mesh. A useful diagnostic to analyze the response of shallow and deep convection to local
460 mesh refinement is the incidence of convection. Because shallow convection in both GF and MSKF is non-
461 precipitating, we set the incidence of shallow convection to 100 % when cloud-tops of shallow convective updrafts
462 are detected, and 0 % otherwise. We set the incidence of deep convection to 100 % when convective precipitation
463 occurs and 0 % otherwise. Figures 6 and 7 highlight the impact of the horizontal scale dependence of convection on
464 the monthly-mean incidence of subgrid-scale shallow and deep convection in our uniform- and variable-resolution
465 experiments for December 2015.

466 Figure 6 shows that simulated shallow convection occurs over the entire Tropical Pacific, and that its incidence
467 is about twice as large in GFu and GFv as in MSKFu and MSKFv. In GFu and GFv, incidence in excess of 48 %
468 covers most of the Tropical Pacific, including the ITCZ and warm pool where GF allows shallow and deep convection
469 to occur simultaneously. GFu and GFv exhibit highest incidence of shallow convection off the coast of Peru where
470 persistent low-level stratiform clouds are formed. In contrast, the incidence of shallow convection in MSKFu and
471 MSKFv never exceeds 32 % over the entire domain and is less than 16 % over the ITCZ and warm pool where shallow
472 and deep convection are not allowed to coexist in MSKF. The bottom panels highlight differences in the incidence of
473 shallow convection between GFv and GFu, and MSKFv and MSKFu. Despite the fact that GF does not include a
474 spatial scale dependence in its formulation of shallow convection, GFv produces reduced shallow convection relative
475 to GFu over most of the Tropical Pacific, except most notably immediately off the coast of Peru. In contrast to GFv,
476 MSKFv yields increased incidence of shallow convection over most of the warm pool region. In MSKF, the height of
477 deep convective clouds decreases as horizontal resolution increases. As the classification between deep and shallow
478 convection is a function of cloud depth, convective clouds originally defined as deep are reclassified as shallow,
479 leading to increased incidence of shallow convection in the refined area of the mesh.

INCIDENCE OF SHALLOW CONVECTION (%)
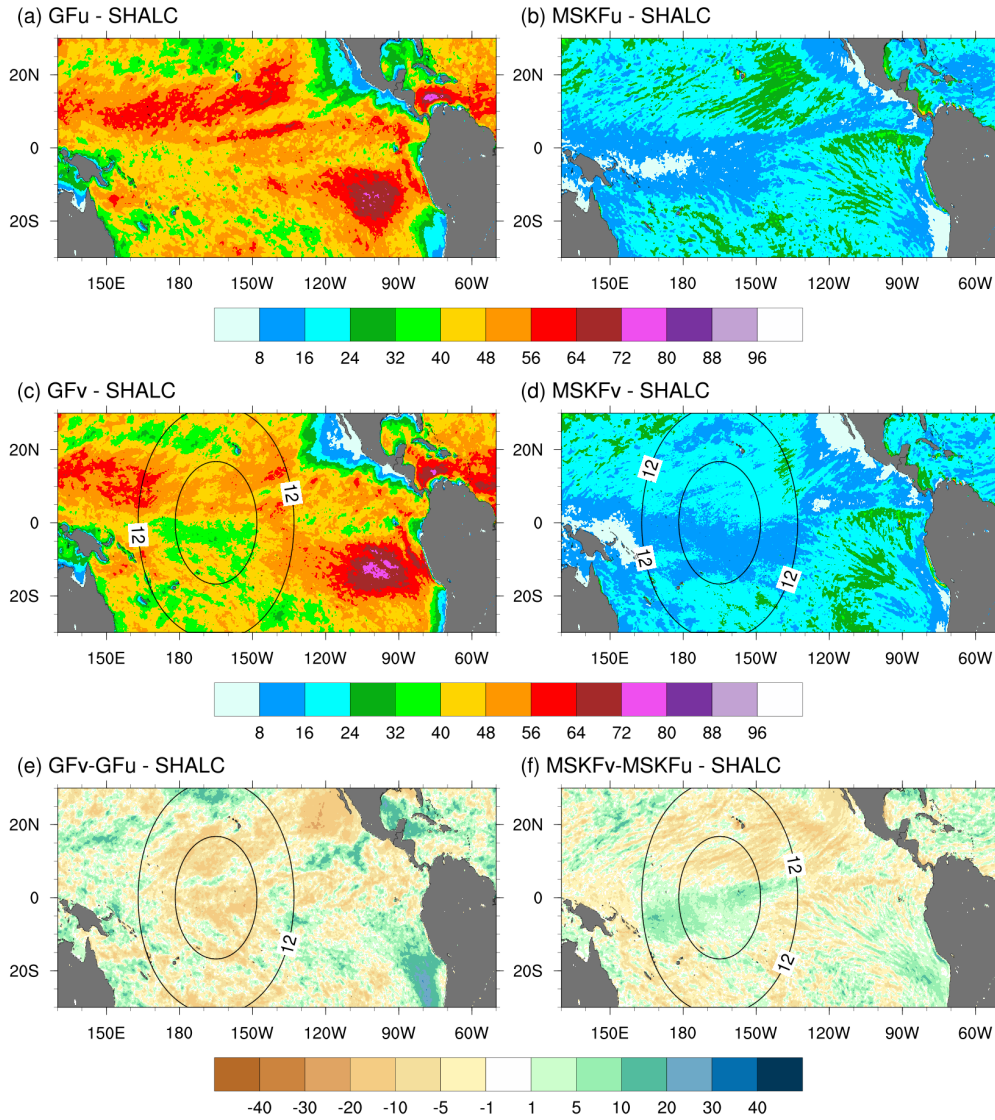
Figure 6: Monthly-mean incidence of shallow convection (SHALC) over the Tropical Pacific Ocean simulated in GFu and MSKFu (top panels) and GFv and MSKFv (middle panels), and difference in the incidence of shallow convection between GFv and GFu (bottom left panel) and MSKFv and MSKFu (bottom right panel) for December 2015.

In Fig. 7, the top and middle panels show that, in contrast to shallow convection, the incidence of deep convection has the same order of magnitude in GFu and MSKFu, and GFv and MSKFv. The top panels reveal that the incidence of deep convection is higher in MSKFu than GFu over the ITCZ and warm pool. In MSKFu, a sharp transition between areas of high and low incidence of deep convection causes areas outside of the ITCZ and warm pool to be mostly void of deep convection, as seen between 10°N and 30°N. In GFu, the incidence of deep convection is decreased over the warm pool relative to the ITCZ west of 160°W. Outside of the ITCZ and warm pool, GFu and GFv lead to higher incidence of deep convection than MSKFu and MSKFv because, in contrast to MSKF, GF allows deep and shallow convection to coexist in the same grid-cell. Middle panels highlight decreased incidence of subgrid-scale deep convection inside the refined area of the mesh over the warm pool in both GFv and MSKFv, as we expect clouds to

493 be resolved on the higher resolution grid, in conjunction with increased incidence east and west of the refined area.
494 The decreased incidence in the refined area is more pronounced between MSKFu and MSKFv than between GFu and
495 GFv whereas the upscaling impact of spatial refinement outside the refined area is greater in GFv than MSKFv. The
496 scale-aware formulation in GF does not produce the same contrast between the refined and coarse mesh in GFv and
497 GFu as that in MSKF in MSKFv and MSKFu. Fig. 7.f reveals a reduced incidence in excess of 25 % between MSKFu
498 and MSKFv starting at resolutions higher than 12 km flanked by increased incidence of deep convection east and west
499 of the refined area. In contrast, Fig. 7.e displays a longitudinal band of decreased incidence of deep convection between
500 90°W and the dateline, bordered by increased deep convection north of the equator and south of 10°S. Table 2 lists
501 the area-averaged incidence of deep and shallow convection for an area inside the refined mesh (REFINED: 0.1°N to
502 5.1°N; 150°W to 180°W) and an area over the Tropical Eastern Pacific (EAST: 3.1°N to 8.1°N; 90°W to 120°W), as
503 later shown in Figure 9.a. The REFINED and EAST areas display little variation in the incidence of shallow
504 convection between GFu (MSKFu) and GFv (MSKFv), but the incidence of shallow convection in GFu and GFv is
505 much higher than in MSKFu and MSKFv. The incidence of subgrid-scale deep convection is higher in the EAST area
506 compared to the REFINED area in all four experiments. Over the REFINED area, the incidence of subgrid-scale deep
507 convection remains about the same between GFu and GFv but strongly decreases between MSKFu and MSKFv.
508

	DEEP CONVECTION (%)		SHALLOW CONVECTION (%)	
	REFINED	EAST	REFINED	EAST
GFu	20	30	52	52
GFv	23	36	47	48
MSKFu	27	33	14	17
MSKFv	10	36	17	15

509 **Table 2:** Area-averaged incidence of deep and shallow convection. The REFINED and EAST areas are shown in Figure 9.a.

510 As described in Section 2, MSKF differentiates shallow from deep convection as a function of the convective
511 cloud depth. As spatial resolution increases, the scale aware formulation leads to a reduction in the intensity of
512 convection and depth of convective clouds, mostly deep convection, over the refined area as seen in Fig. 7.f. As the
513 depth of convective clouds originally classified as precipitating deep convective clouds become shallower, MSKF
514 reclassifies those same clouds as nonprecipitating shallow clouds, leading to near-equal compensation between the
515 decreased and increased incidence of deep and shallow convection over the warm pool. In contrast to MSKF, GF
516 causes precipitating deep convection to become precipitating shallow convection at increased spatial resolution. As
517 this process occurs in the deep convection scheme and both cloud types precipitate, variations in the incidence of deep
518 convection between GFu and GFv are small. Further analysis of the response of shallow convection between GFu and
519 GFv over the refined area is beyond the objectives of this research.

INCIDENCE OF DEEP CONVECTION (%)

(a) GFu - DEEPC

(b) MSKFu - DEEPC

(c) GFv - DEEPC

(d) MSKFv - DEEPC

(e) GFv-GFu - DEEPC

(f) MSKFv-MSKFu - DEEPC
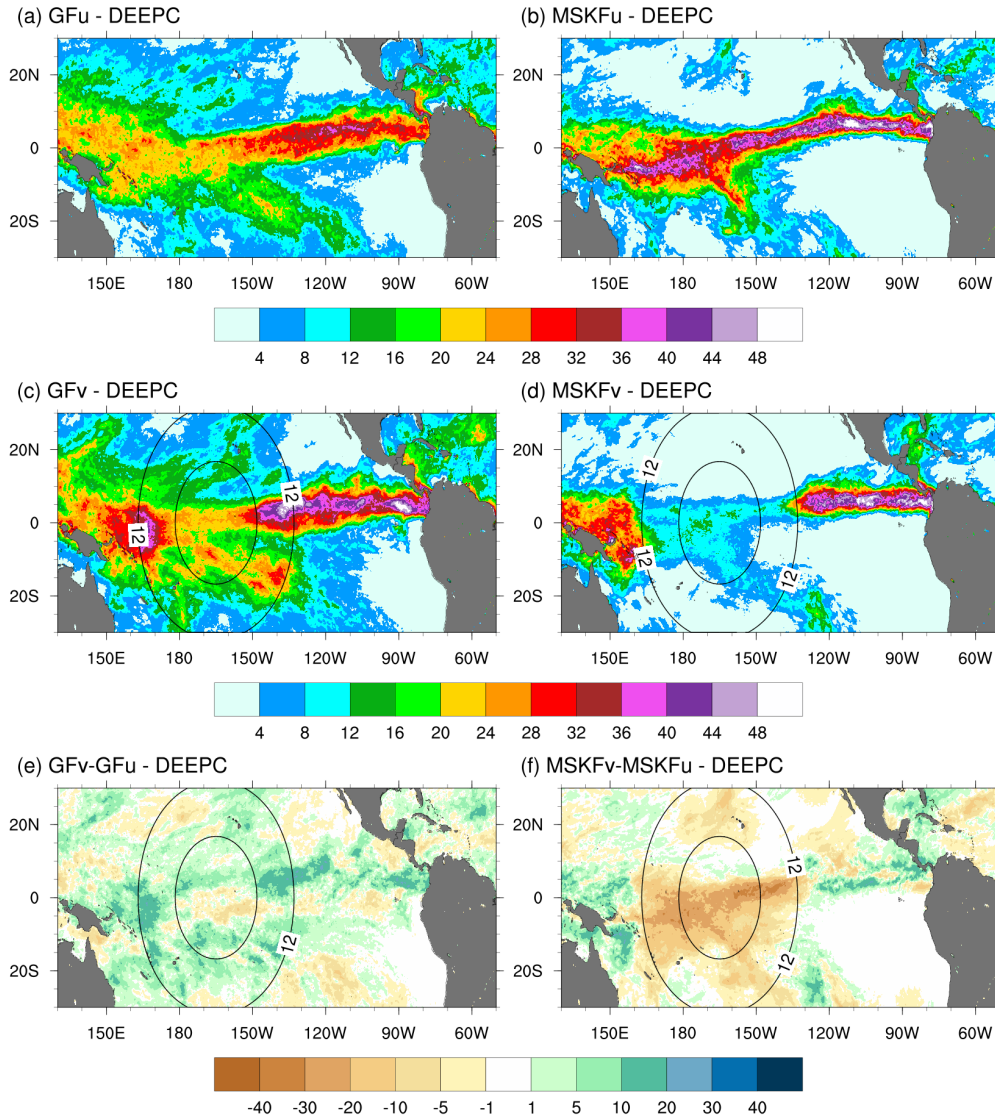
Figure 7: As Fig. 6, but for the monthly-mean incidence of deep convection (DEEPC).

4.2 Precipitation rates

Figure 8 shows the monthly-mean convective precipitation rate simulated in GFu and MSKFu (top panels), and GFv and MSKFv (middle panels). The bottom panels in Figure 8 display the ratio between the convective precipitation rate simulated in GFv (MSKFv) and GFu (MSKFu) to contrast the impact of the scale aware formulation in GF and MSKF. The top panels highlight similar geographical patterns of convective precipitation in GFu and MSKFu. Between 80°W and 160°W, increased convective precipitation is located along the ITCZ, in conjunction with increased incidence of deep convection, as seen in Figs. 7.a-b. West of 160°W, GFu leads to decreased but more widespread convective precipitation relative to MSKFu over the warm pool, in conjunction with decreased but more widespread incidence of convection. In GF, this result infers that while deep convection is not triggered as often over the warm pool as along the ITCZ, the amount of convective precipitation produced in one time-step is higher over the

532 warm pool than along the ITCZ, so that monthly-mean convective precipitation rates remain about the same in both
533 regions. In Fig. 8, and in agreement with the middle panels of Fig. 7, middle panels display a strong decrease in
534 convective precipitation in both GFv and MSKFv over the refined area of the mesh. In MSKFv, the strong reduction
535 in convective precipitation occurs, not only over the most refined area of the mesh, but also where horizontal grid-
536 spacing increases from 6 to 12 km. In GFv, convective precipitation increases sharply as soon as grid-spacing is greater
537 than 12 km and exceeds that simulated in GFu over the coarse area of the mesh. In GFv, the monthly-mean convective
538 precipitation rate is higher than that in MSKFv over the most refined area of the mesh but starts to increase more
539 rapidly between 6 and 12 km than in MSKFv. Differences in increasing convective precipitation across the transition
540 zone between the refined and coarse areas reflect different impacts of the scale-aware formulation in GF and MSKF.
541 The bottom panels in Figure 8 show that the ratio in convective precipitation between GFv and GFu has the same
542 order of magnitude as that between MSKFv and MSKFu over the refined area of the mesh. While it remains as small
543 in the transition zone as in the refined mesh with MSKF, this ratio increases to values greater than 1 between 6 and
544 12 km with GF, indicating increased convective precipitation on each side of the refined area in GFv relative to GFu,
545 as also seen in Figure 8.c. Maps of monthly-mean grid-scale precipitation rates show similar geographical patterns
546 between GFu and MSKFu. Over the refined area, increased grid-scale precipitation compensates decreased convective
547 precipitation in both GFv and MSKFv. Over the coarse area, grid-scale precipitation decreases along the ITCZ and
548 warm pool in GFv while remaining nearly the same in MSKFv (not shown for brevity).

CONVECTIVE PRECIPITATION RATE (mm day⁻¹)
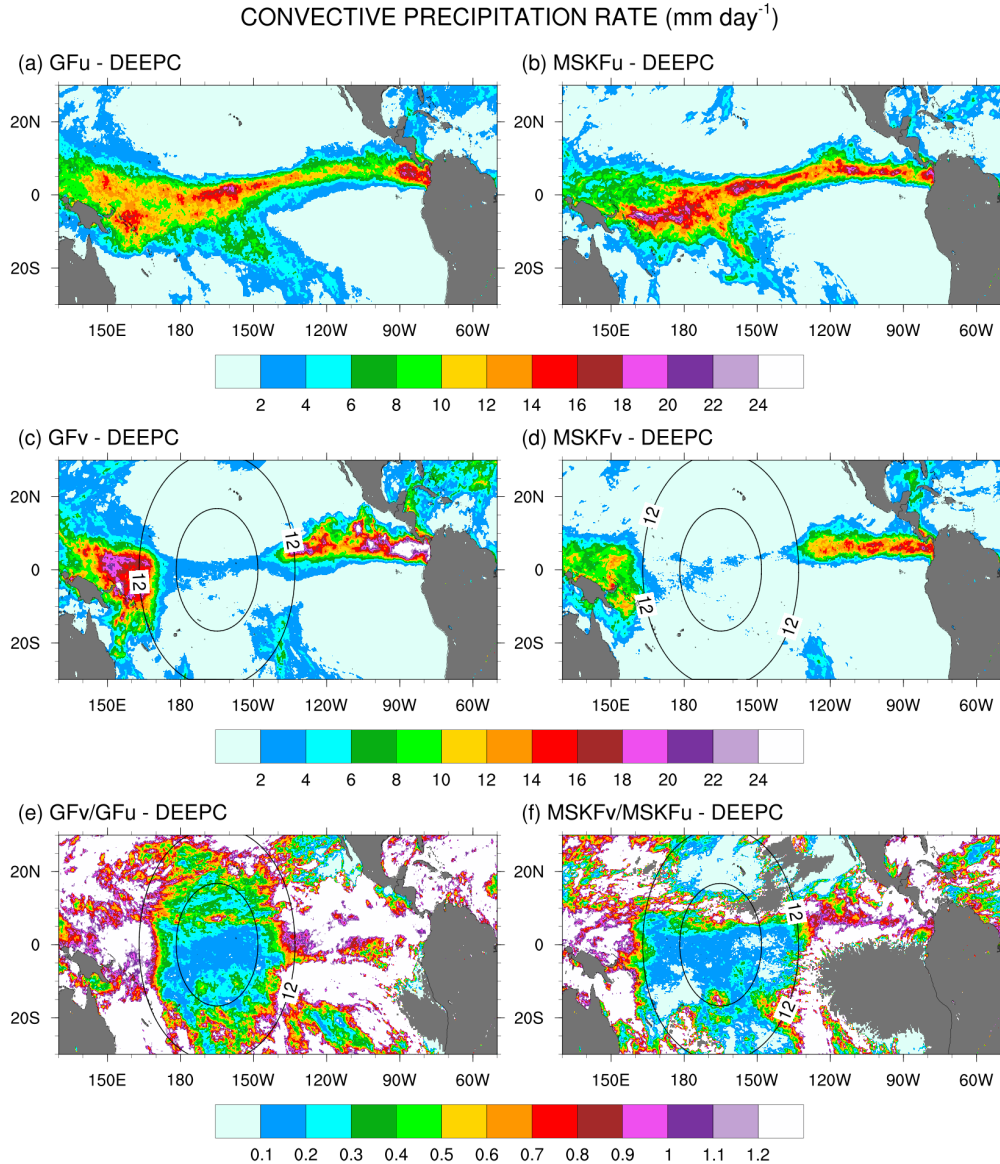
549
550 **Figure 8:** Monthly-mean convective (DEEPC) precipitation rate over the Tropical Pacific Ocean simulated in GFu and MSKFu
551 (top panels), GFv and MSKFv (middle panels), and ratio between the monthly-mean convective precipitation rate in GFv (MSKFv)
552 and GFu (MSKFu) for December 2015.

553   The simulated total precipitation rate can be compared to observed TMPA precipitation using Figs. 9 and 10

554 which show the precipitation rates and differences between simulated and observed precipitation rates, respectively.

555 Areas of maximum satellite-retrieved precipitation are found over the ITCZ between 130°W and the dateline (Fig.

556 9.a). Observed precipitation decreases over the warm pool west of the dateline and decreases strongly over the Tropical

557 Eastern Pacific (between 80ºW and 120ºW) and the SPCZ. The four simulations overestimate precipitation in the

558 Tropical Eastern Pacific between 80ºW and 120ºW (Figs. 9.b-e) with biases in excess of 11 mm day⁻¹ (Figs. 10.a-d).

559 The four simulations also overestimate precipitation between 130ºE and 160ºE, or west of the refined area, with biases

560 about as large as those seen east of the refined area, except for MSKFu. The uniform-grid results (Figs. 9.b-c) display

561 the highest precipitation rates over the area of warmest SSTs where we expect deepest convection to occur and are in

562 reasonable agreement with TMPA data. However, GFu and MSKFu locate the ITCZ south of its observed location

563 (Figs. 10.a-b), producing a positive bias straddling the Equator and a negative bias north of the Equator. The scale-

564 aware dependence of deep convection in GF leads to decreased total precipitation in GFv compared to GFu over the

565 entire refined area (Fig. 10.e). In contrast, Fig. 10.f shows that while the scale-aware dependence in MSKF leads to

566 decreased precipitation in MSKFv over a major fraction of the refined area, it also leads to an improved location of

567 the simulated ITCZ, as evidenced by increased precipitation north of the Equator.
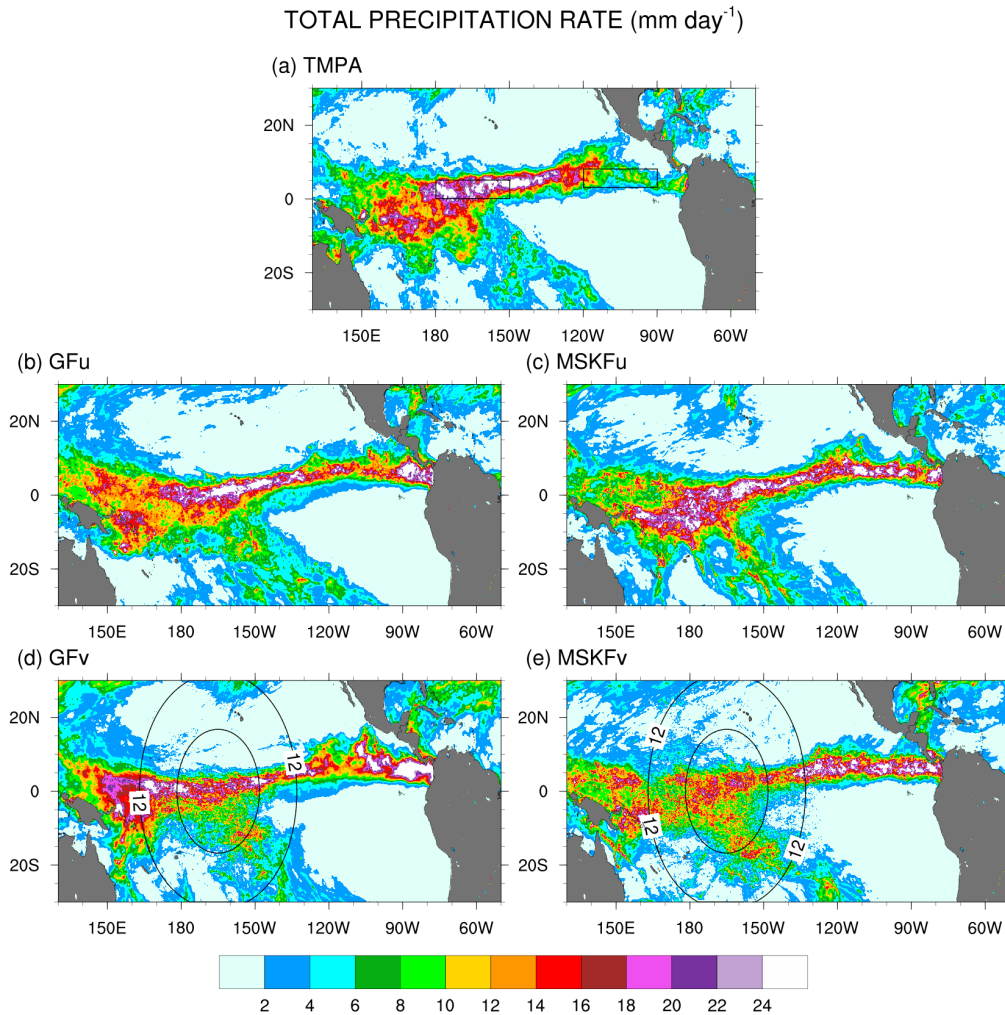
568
569 **Figure 9:** Monthly-mean total precipitation rate over the Tropical Pacific Ocean from TMPA data (top panel) and simulated with
570 GFu and MSKFu (middle panels) and GFv and MSKFv (bottom panels) for December 2015.

571   Table 3 summarizes the area-mean monthly-mean convective, grid-scale, and total simulated and observed TMPA

572 precipitation rates over the REFINED and EAST areas. Over the two areas, the simulated total precipitation is about

573 the same for all four experiments but is underestimated (overestimated) relative to TMPA data over the REFINED

574 (EAST) areas, respectively. Over the REFINED area, total precipitation decreases by 2.1 mm day^{-1} between GFu and

575 GFv and 2.3 mm day^{-1} between MSKFu and MSKFv, highlighting a near-equal compensation between decreased deep

576 convective and increased grid-scale precipitation over the most refined area of the mesh. Over the EAST area, total

577 precipitation increases by 2.7 mm day^{-1} between GFu and GFv resulting from a 5.3 (2.6) mm day^{-1} increase (decrease)

578 in convective (grid-scale) precipitation. In contrast, total precipitation increases by 1.2 mm day^{-1} between MSKFu and

579 MSKFv resulting from a 0.5 (0.6) mm day^{-1} increase in convective (grid-scale) precipitation. The large (small) increase

580 in convective precipitation in GFv (MSKFv) over the coarse areas east (and west) of the refined area highlights distinct

581 upscaling effect of the refined area on the coarse area of the mesh between GFv and MSKFv.

PRECIPITATION RATE DIFFERENCE (mm day^{-1})
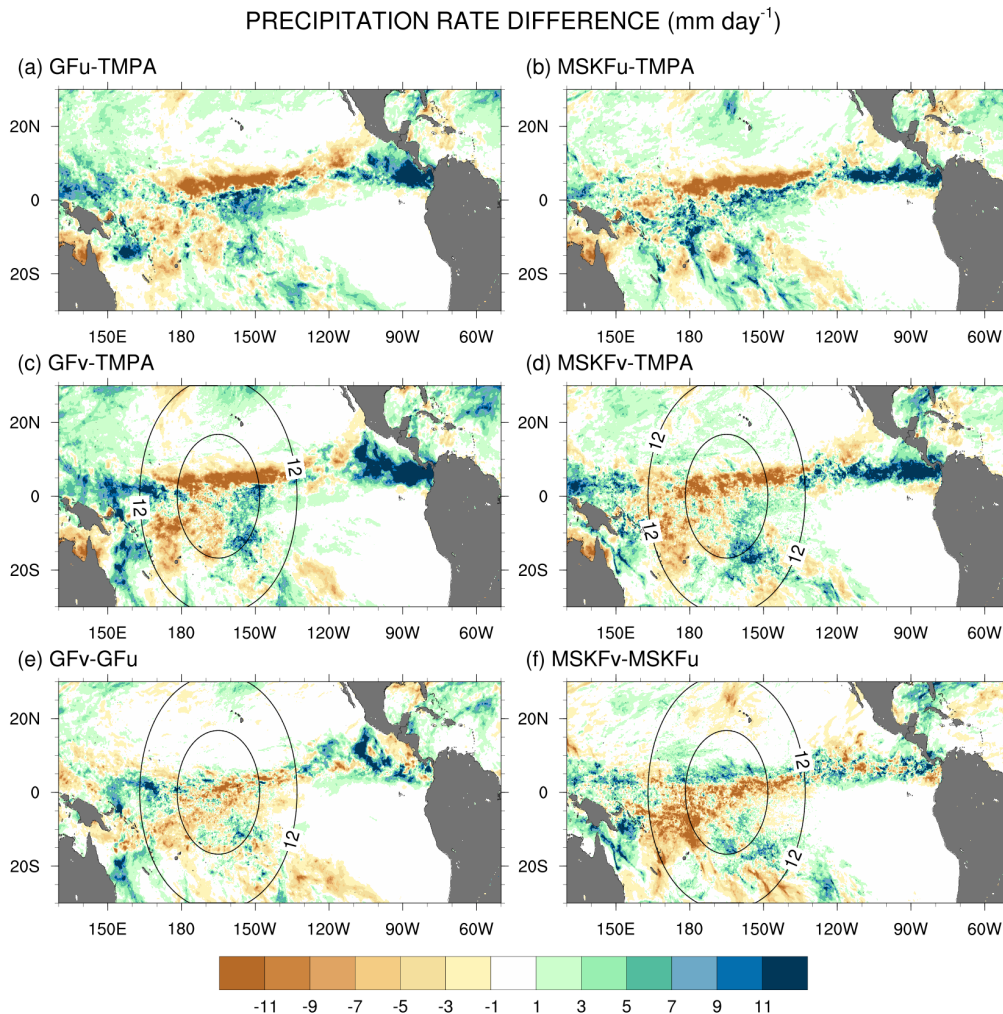
582
583 **Figure 10:** Monthly-mean precipitation rate difference over the Tropical Pacific Ocean between GFu (MSKFu) and TMPA data
584 (top panels), GFv (MSKFv) and TMPA data (middle panels), and between GFv (MSKFv) and GFu (MSKFu) (bottom panels) for
585 December 2015.

586   In summary, the scale dependence of convection in GF and MSKF produces the same partitioning between

587 convective and grid-scale precipitation inside the refined area or decreased convective and compensating increased

588 grid-scale precipitation as horizontal resolution increases. The upscaling impact on convective and grid-scale

589 precipitation varies between GF and MSKF. As seen in Fig. 8 and Table 3, convective precipitation increases strongly

590 over the warm pool and Eastern Pacific starting across the transition zones east and west of the refined area in GFv.

591 In contrast, while the parameterization of the scale dependence of deep convection in MSKF produces a stronger

592 decrease in convective precipitation in MSKFv than GFv, it produces a smoother transition in convective precipitation

593 and decreased upscaling effect as spatial resolution reaches 30 km.

594

	CONVECTIVE (mm day^{-1})		GRID-SCALE (mm day^{-1})		TOTAL (mm day^{-1})	
	REFINED	EAST	REFINED	EAST	REFINED	EAST
GFu	10.0	8.7	6.1	3.7	16.1	12.4
GFv	1.9	14.0	12.1	1.1	14.0	15.1
MSKFu	10.9	10.6	4.9	4.8	15.8	15.5
MSKFv	1.7	11.1	11.8	5.4	13.5	16.5
TMPA					20.7	7.3

595 **Table 3:** Area-averaged convective, grid-scale, and total precipitation rates over the same areas as those described for Table 2. The
596 REFINED and EAST areas are shown in Figure 9.a.

5 Simulated relative humidity and simulated versus satellite-retrieved LWP and IWP

5.1 Relative humidity

599 One effect of local mesh refinement is the decreased contribution of parameterized convection compensated by
600 increased contribution of grid-scale cloud microphysics to condensation processes and cloud formation with
601 increasing spatial resolution. Therefore, prior to comparing the simulated LWP and IWP against SSF data, we first
602 investigate differences in relative humidity (RH) between our uniform- and variable-resolution experiments. Figure
603 11 displays the monthly-mean longitude-pressure cross sections of RH latitudinally-averaged between 5°S and 5°N.
604 East of 150°W over the Tropical Eastern Pacific, the four experiments display similar vertical distributions of RH,
605 with relatively lower RH between 700 hPa and 150 hPa and higher RH in the PBL below 700 hPa and in the upper-
606 troposphere above 150 hPa. All four experiments show significant increase in RH west of 150°W across the entire
607 troposphere, over the warm pool where the warmest SSTs are seen (Fig. 2.a) and deepest convective updrafts are
608 formed. Comparing GFu against MSKFu over the warm pool shows that GF has stronger drying than MSKF in the
609 lower troposphere, leading to a lower RH between 850 hPa and 300 hPa in GFu than MSKFu. In addition, GF produces
610 stronger moistening than MSKF in the upper troposphere leading to a higher RH between 300 hPa and 100 hPa in
611 GFu than MSKFu. As seen in the bottom panels of Fig. 11, reducing parameterized deep convection while enhancing
612 grid-scale cloud microphysics produces a higher RH over the refined area in GFv and MSKFv, but without
613 significantly modifying RH over the coarse area of the mesh. Variations in the vertical distribution of RH at pressures
614 less than 400 hPa are more pronounced between GFu and GFv than between MSKFv and MSKFu. Because the cloud
615 fraction (CF) is a function of RH, as described in Xu and Randall (1996; Eq. 1), there is a strong relationship between
616 the longitude-pressure cross sections of RH and CF, as seen in Fig. S2 (see supplemental figures). The highest CF
617 coincide with the highest RH at about 100 hPa over the warm pool in all four experiments. As for RH, GFu and GFv
618 display higher and lower values of CF than MSKFu and MSKFv in the upper and lower troposphere. The top and
619 bottom panels of Fig. S3 show differences in RH and CF between GFv and GFu, and between MSKFv and MSKFu.
620 One notable difference is a stronger increase in upper-tropospheric clouds between MSKFu and MSKFv than between

621 GFv and GFu, particularly over the refined area of the mesh. While increased grid-scale condensation over the refined

622 area impacts the entire tropospheric in GFv, it more strongly affects the upper-troposphere in MSKFv.
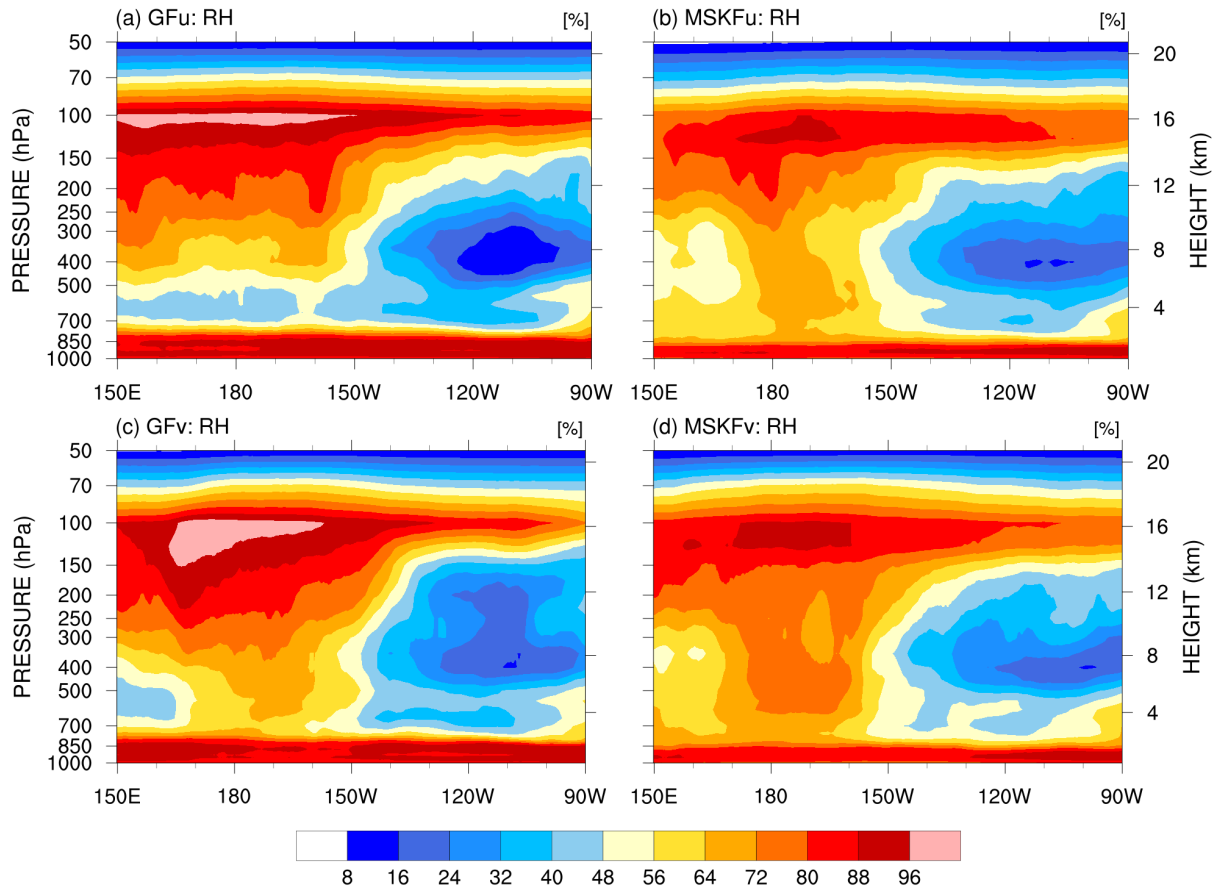
623
624 **Figure 11:** Longitude versus pressure cross-section of latitudinally-averaged (between 5°S and 5°N) relative humidity (RH) across
625 the Tropical Pacific Ocean simulated in GFu and MSKFu (top panels) and GFu and GFv (bottom panels) for December 2015.

626   To explain the change in RH over the refined area between the uniform- and variable-resolution experiments, we

627 compare the monthly-mean upward moisture flux at 850 hPa and 200 hPa between MSKFu and MSKFv over the

628 Tropical Eastern Pacific (Fig. 12). There is a significant decrease in the upward moisture flux between 850 hPa and

629 200 hPa in conjunction with decreased specific humidity with height in MSKFu and MSKFv (Fig. 11). As seen in the

630 top panels of Fig. 12, MSKFu yields highest values of the upward moisture flux along the ITCZ and over the warm

631 pool in association with parameterized deep convection. Outside the ITCZ and warm pool, lower values of the upward

632 moisture flux at 850 hPa result because of reduced deep convection in conjunction with shallow convection, as seen

633 over the SPCZ. At increased spatial resolution, convective processes transition from being parameterized to resolved,

634 producing larger grid-scale vertical velocities, stronger upward moisture flux, and increased grid-scale condensation

635 through the entire troposphere over the refined area of the mesh. Comparing the bottom versus top panels of Fig. 12

636 outlines the intensification of vertical moisture transport at both pressure levels over the refined area, leading to the

637 increased relative humidity with increased spatial resolutions shown in Fig. 11.
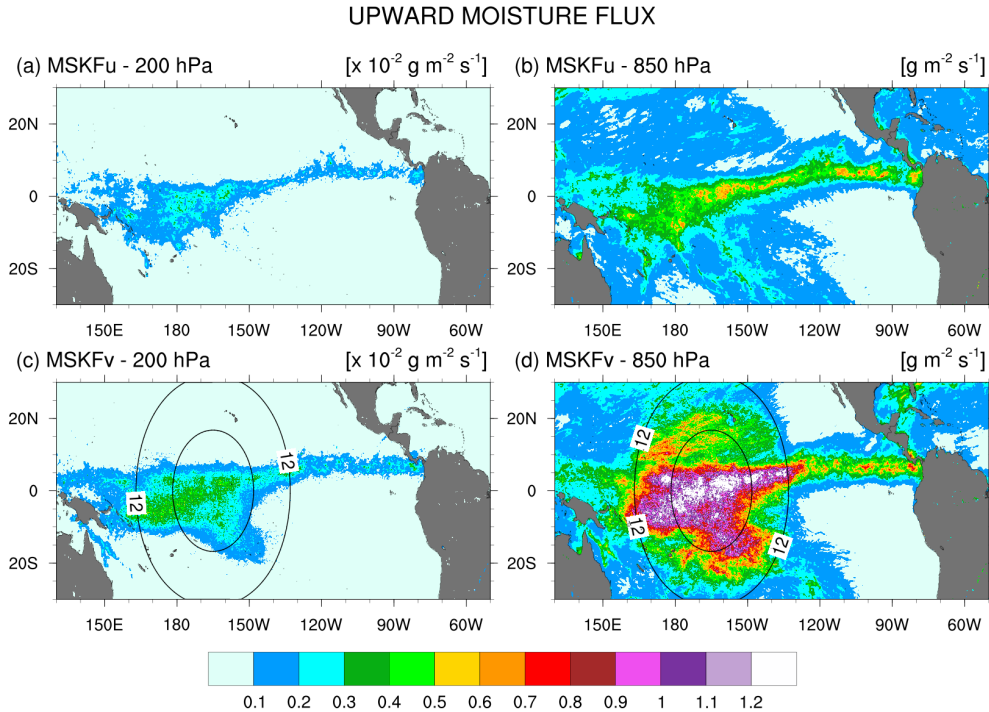
UPWARD MOISTURE FLUX

Figure 12: 200 hPa (left panels) and 850 hPa (right panels) monthly-mean upward moisture flux simulated with MSKF over the Tropical Pacific Ocean for December 2015. Top panels (a) and (b) are for MSKFu and bottom panels (c) and (d) are for MSKFv. Note the 1x10^{-2} scaling between 200 hPa and 850 hPa.

5.2 Liquid Water Path (LWP)

Figure 13 displays difference maps between the simulated and satellite-derived LWP, and between GFv (MSKFv) and GFu (MSKFu). In Fig. 13, the simulated LWP is calculated using only the grid-scale cloud liquid water mixing ratio from THOM. Separate analyses would show that adding the prognostic grid-scale rain mixing ratio to the simulated LWP further increases biases when compared against the SSF LWP (not shown for brevity). We also do not include the contribution of the convective cloud liquid water mixing ratio to the LWP which is small compared to that from the grid-scale cloud microphysics. Figure 13 highlights that GFu strongly overestimates the LWP over the ITCZ, and between 20°N (20°S) and the northern (southern) limits of our analysis. As seen in Fig. 6, GFu attempts to form low-level boundary layer clouds off the coast of Peru but these clouds form too far west from the coast when compared against observations. This same bias is depicted in Fig 13.a since these low-level boundary layer clouds are characterized by high LWP. In Fig. 13.b, decreased bias between the MSKFu and SSF LWP reflects that the LWP is strongly decreased in MSKFu compared to GFu, outside of the areas of low-level boundary layer clouds. If we set aside that MSKFu is unable to simulate low-level clouds off the Baja Peninsula and coast of Peru, the magnitude and regional patterns of the LWP simulated in MSKFu is in fairly good agreement with the SSF LWP. Because MSKF does not allow deep and shallow convection to coexist within the same grid-cell and deep convection dominates shallow convection over the ITCZ and warm pool, we suggest that detrained cloud water from deep convection as a source to grid-scale microphysics contributes a major part to the LWP produced by MSKFu. The bottom panels of Fig. 13 reveal that the mesh refinement impacts the LWP simulated with MSKF more effectively than that simulated

660 with GF inside the refined area. This result is in agreement with the stronger increase in RH between MSKFu and
661 MSKFv than between GFu and GFv at lower levels. MSKFv yields an increased LWP relative to MSKFu over the
662 entire refined area (Fig. 13.f). MSKFv also has increased LWP compared to MSKFu over the coarse area, but not as
663 large as that seen over the refined area. Figure 13.e shows that the LWP differences do not have a strong positive or
664 negative trend inside the refined area, due to the fact that GF allows deep and shallow convection to coexist within
665 the same grid-cell of deepest convective activity, mainly over the ITCZ and warm pool, and shallow convection does
666 not account for variations in horizontal grid-spacing. Over the coarse area, an obvious decrease in the LWP between
667 GFv and GFu is seen over the ITCZ in the Tropical Eastern Pacific as well as along the southern boundary of our
668 analysis.
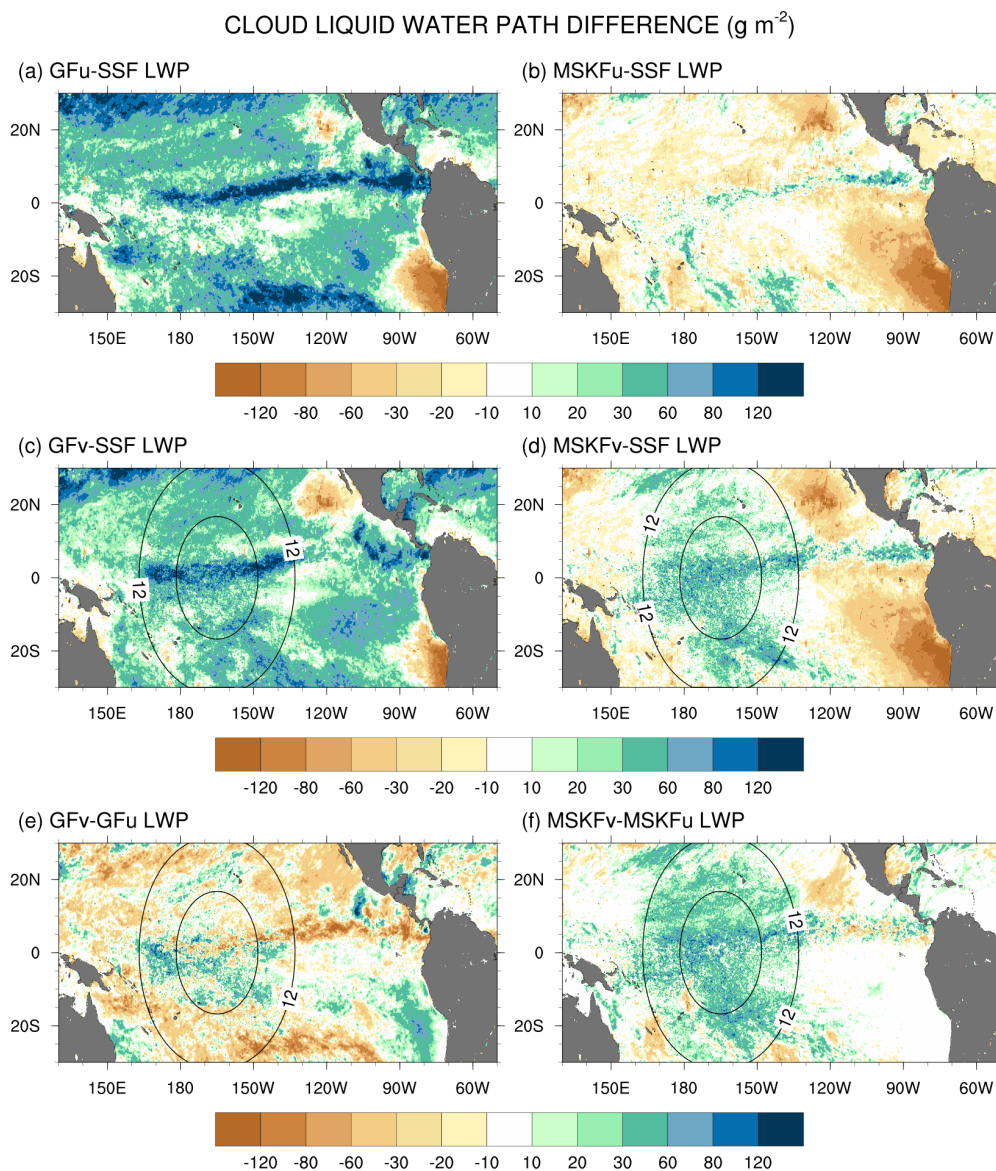
669
670 **Figure 13:** Monthly-mean cloud liquid water path (LWP) difference over the Tropical Pacific Ocean between GFu (MSKFu) and
671 SSF data (top panels), GFv (MSKFv) and SSF data (middle panels), and monthly-mean LWP difference between GFv (MSKFv)
672 and GFu (MSKFu) (bottom panels) for December 2015.

673   In order to investigate the reasons why the LWP simulated in GFu strongly exceeds that from the SSF products
674   and MSKFu, we calculate the monthly-mean LWP produced in grid-cells with incidence of deep convection, shallow
675   convection, and no convection, using LWP hourly outputs from GFu. Separate maps show that a major fraction of the
676   LWP over convectively active regions such as the ITCZ is actually produced at times when no convection is active or
677   when only shallow convection is triggered (not shown for brevity). In GF, and in contrast to deep convection, shallow
678   convection detrains total water as a source of grid-scale water vapor instead of detraining water vapor, cloud liquid
679   and ice water, separately. Because the detrained total water is treated as a source of water vapor, supersaturation
680   conditions are more likely to persist and later removed by grid-scale condensation. In contrast, detrainment from deep
681   convective updrafts acts as a source of liquid water if temperatures are warmer than 258 K. Deep convection in
682   conjunction with grid-scale condensation contributes the least to the LWP because updrafts are taller and their cloud-
683   top temperatures colder than those from shallow convection, leading to condensation and deposition to occur at levels
684   where temperatures are colder than 258 K, and where ice phase processes dominate.

685   The impact of more active shallow convection in GFu (GFv) than in MSKFu (MSKFv) is analyzed using Fig. 14
686   which shows differences in the monthly-mean precipitable water below 700 hPa between our experiments and ERA-
687   Interim reanalyses. Because varying horizontal resolution does not affect shallow convection, GFv (MSKFv) displays
688   similar biases as GFu (MSKFu) over the entire analysis domain, including the refined area. Comparing the left versus
689   right panels of Figure 14 reveals that the precipitable water simulated in GFu (GFv) displays a positive bias whereas
690   that simulated in MSKFu (MSKFv) displays a negative bias in the lower troposphere relative to ERA-Interim data,
691   mainly over areas of shallow convection. In GF, the abundance of shallow convection (Figure 6.a, Figure 6.c)
692   associated with detrained total water acting as a source of grid-scale water vapor promotes the lower troposphere to
693   stay more humid and cloud liquid water to form more often than actually observed (Figure 13.a, Figure 13.c), north
694   and south of the ITCZ and warm pool. In MSKF, while shallow convection is as widespread over the Tropical Pacific
695   Ocean as in GF, it cannot act as a major source of detrained total water to the grid-scale microphysics because it is not
696   triggered as often as deep convection. In addition, because MSKF partitions detrained water into water vapor, cloud
697   water, cloud ice, rain, and snow, instead of detraining total water in the form of water vapor as in GF, the amounts of
698   available water vapor and cloud liquid water are reduced relative to GF.

PRECIPITABLE WATER BELOW 700 hPa (kg m^{-2})
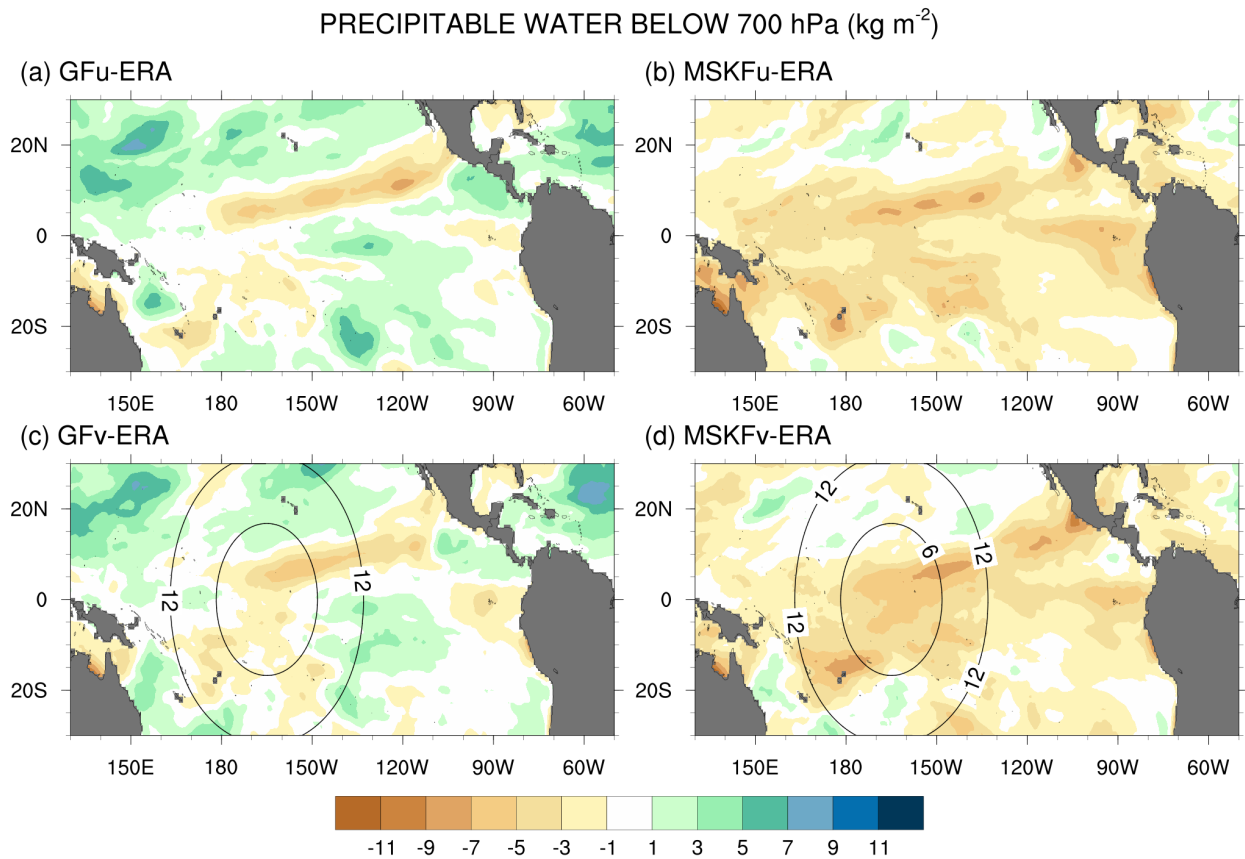
Figure 14: Monthly-mean difference between the simulated and ERA-Interim precipitable water below 700 hPa over the Tropical Pacific Ocean for December 2015.

5.3   Ice Water Path (IWP)

Because MODIS is relatively insensitive to precipitation, the simulated IWP should comprise cloud ice, snow, and graupel. Because graupel contributes a minor part to the IWP relative to cloud ice and snow and our results highlight strong biases against SSF data, we do not include graupel in our computation of the simulated IWP. It is also important to note that because THOM has the propensity to rapidly convert cloud ice to snow (Thompson et al. 2016), most of the IWP is in the form of snow which falls at higher speeds than cloud ice, enhancing the depth of ice clouds. Lastly, the middle panels of Fig. 5 show that our gridding of the IWP orbital data produce increased monthly mean IWP than the official SSF1deg product. This result implies that biases between the simulated and satellite-derived IWP will be underestimated when using our SSF 0.2°x0.2° IWP data. Figure 15 shows difference maps between the simulated and satellite-derived IWP, and between GFv (MSKFv) and GFu (MSKFu). When compared against the SSF IWP, GFu is the only experiment that mostly underestimates the IWP along the ITCZ and warm pool whereas GFv yields a strong increase in the IWP over the refined area of the mesh relative to GFu. Both GFu and GFv overestimate the IWP along the west coast of Central America, as they did for the LWP and precipitation. Comparing MSKFu (MSKFv) against GFu (GFv) shows that MSKF leads to increased positive biases in the IWP compared to GF over

716 the entire ITCZ and warm pool. Increased convective detrainment of cloud ice as a source of grid-scale cloud ice to

717 THOM in MSKF than in GFv, because partitioning between cloud liquid and ice water starts at warmer temperatures,

718 may be responsible to the increased IWP. The bottom panels of Figure 15 reveal that increasing spatial resolution

719 worsens the simulated IWP compared to the SSF IWP over the refined area in GFv and MSKFv. As shown in Fig. 11,

720 mesh refinement over the warm pool yields higher upper-tropospheric relative humidity leading to increased ice cloud

721 microphysics. In contrast to GFv, MSKFv displays an increase in the IWP over the coarse area of the mesh, showing

722 a stronger impact of the refined area on the coarse area of the mesh in MSKFv than GFv in the upper-troposphere.

CLOUD ICE WATER PATH DIFFERENCE (g m^{-2})
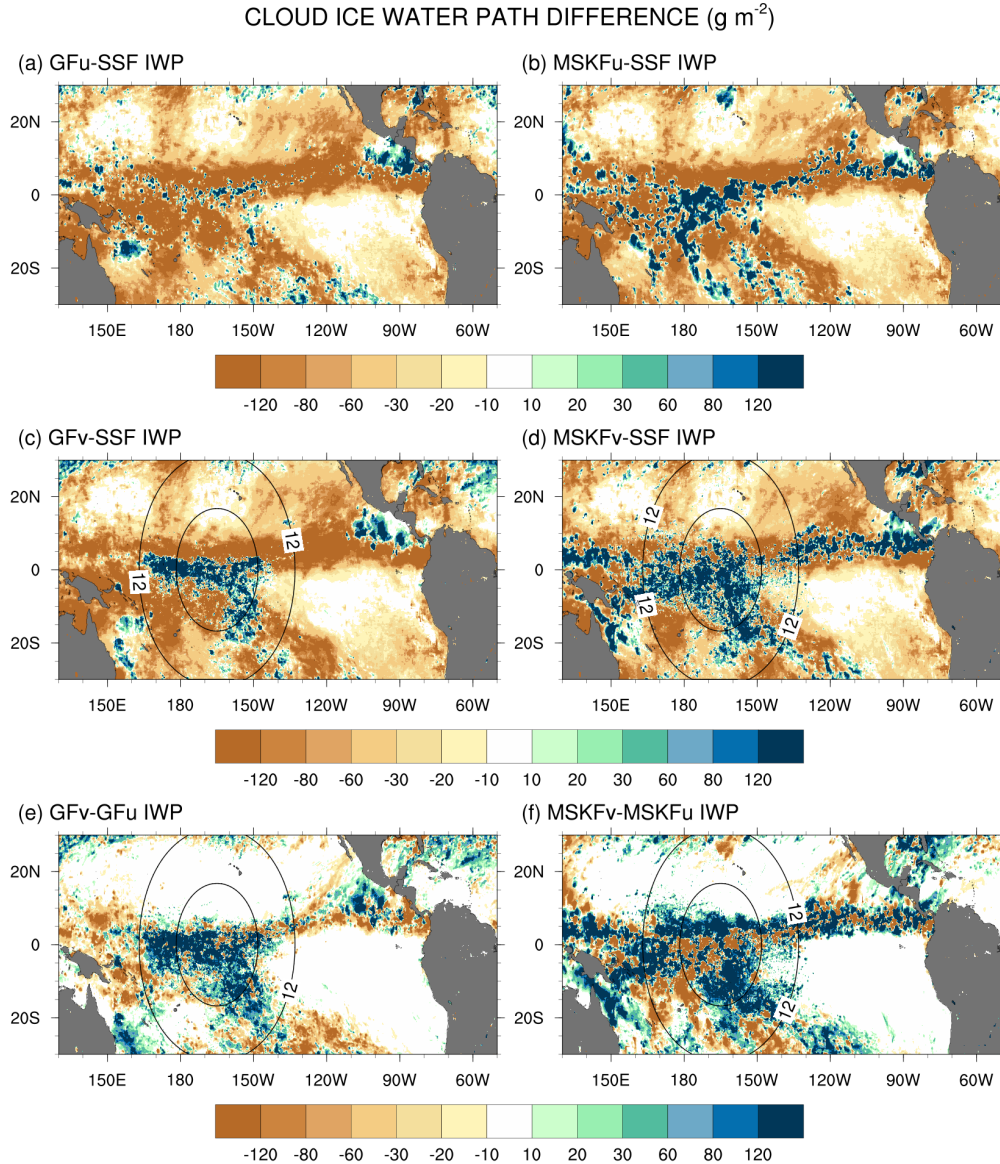
723

724 **Figure 15:** As Fig. 13, but for the cloud ice water path (IWP).

725 **5.4 TOA radiation budget**

726   Biases in the LWP and IWP introduce biases in the cloud fraction and cloud optical properties which in turn lead

727 to biases in the simulated TOALW and TOASW compared to CERES-SSF data. Figures S4, S5, and S6 display the

728 monthly-mean CF, TOALW, and TOASW from SSF data for December 2015 and the differences between the model
729 results and observations. Focusing on areas of deep convection over the ITCZ and warm pool, all four simulations
730 overestimate CF with larger biases seen in the GF than the MSKF experiments, and larger biases seen in the variable-
731 resolution than the uniform-resolution experiments. All four simulations also overpredict CF along the west coast of
732 Central America while underpredicting CF over areas of stratiform clouds along the west coast of South America and
733 Baja Peninsula. The impact of CF biases is that all four experiments underestimate the size of the warm pool and
734 width of the ITCZ, leading the TOALW (TOASW) to be too high (low) over areas of deep convection. These
735 differences are clearly linked to the differences noted in the LWP and IWP between MPAS and SSF data.

736 **6   Discussion**

737   When running GFu (MSKFu) and GFv (MSKFv), we set the time-step to be as large as possible to reduce the
738 computational cost of the various experiments without compromising computational stability. Using decreased time-
739 steps between the quasi- and variable-resolution experiments from 150 s to 30 s implies that it is not possible to directly
740 compare the mean state of GFv (MSKFv) against that of GFu (MSKFu) in the coarse area of the variable-resolution
741 mesh, and upscale effects of local mesh refinement. This is in contrast to Sakaguchi et al. (2015) and Hagos et al.
742 (2013) who constrain the time-step to be the same at all horizontal scales, allowing their study to assess the upscale
743 effect of mesh refinement across the transition zones between the refined and coarse areas of the mesh, and far from
744 the refined mesh. In order to understand the increase in convective precipitation east and west of the transition zones
745 in GFv relative to GFu, we run GFu with the reduced 30 s time-step to quantify the dependence of convective
746 precipitation to the dynamic time-step. As seen in Fig. S7.a (S7.b), reducing the time-step from 150 s to 30 s strongly
747 increases convective precipitation over convectively active regions of the Tropical Pacific Ocean, highlighting the
748 sensitivity of GF to the time-step. Reducing the time-step in MSKFu yields convective precipitation differences that
749 are not as large as those seen in Fig. S7.b (not shown for brevity). Using the Community Atmosphere Model Version
750 4 (CAM4) with a T340 spectral truncation and a 5 min time-step, Williamson (2013) demonstrates the dependence of
751 the removal of supersaturation conditions to the shallow (30 min) and deep (1 h) convective time-scales. While it is
752 important to point out that the sensitivity studies discussed in Williamson (2013) depend on the CAM4 coupling
753 between the convective and grid-scale cloud parameterizations and the dynamical core, shorter convective time-scales
754 relative to the time-step yield faster removal of moist instabilities through vertical motions and condensation. In GF,
755 the time-scales used in the *AS* and *KF* closures are set to the dynamical time-step and 20 min, respectively. While the
756 contribution of the *KF* closure decreases by a factor of 5 in response to the decreased time-step, the contribution of
757 the *AS* closure is independent of the convective time-scale but will affect the cloud base mass flux through variations
758 in the cloud work function. In order to further understand the impact of the time-step on increased supersaturation and
759 convective precipitation in GF, a detailed analysis of the contributions of the dynamics and physics forcing on the *AS*
760 cloud work function in MPAS is needed. This is the object of future research.

7   Summary and future research

Uniform- and variable-resolution experiments with two scale-aware parameterizations of deep convection (GF and MSKF) in MPAS yield significant biases between the simulated and satellite-derived monthly-mean precipitation rates, LWP, IWP, and CF over the Tropical Pacific Ocean for December 2015. In turn, biases affect the cloud fraction and optical properties producing significant differences in the TOALW and TOASW compared to CERES-SSF data.

Tropical precipitation simulated with uniform-resolution experiments is overestimated compared to TMPA, due to subgrid-scale deep convection. Biases using GF are as large as those using MSKF, and result in part because the simulated ITCZ is located south of its observed location. Variable-resolution experiments do not produce significant improvement in simulating precipitation against TMPA. Inside the refined area, decreased convective precipitation plus compensating increased grid-scale precipitation have the simulated total precipitation to exhibit similar biases between the uniform- and variable-resolution experiments with GF and MSKF. One major difference in using GF instead of MSKF is the strong upscaling effect of the refined mesh on the coarse mesh, producing a strong increase in convective precipitation east and west of the refined mesh. Because deep convection does not exhibit similar behaviour over the transition zone between the coarse and refined areas of the mesh in MSKF, we plan further to investigate this difference in convective precipitation in terms of the size of convective updrafts as a function of horizontal resolution and increased moistening of the lower troposphere from shallow convection.

Differences in the simulated LWP between the uniform- and variable-resolution experiments using GF and MSKF and against the CERES-SSF LWP highlight the need to revise the treatment of shallow convection to improve warm-phase clouds in both schemes. While experiments using MSKF yield the simulated LWP to be in reasonable agreement against that from the CERES-SSF product, those using GF yield the simulated LWP to be strongly overestimated. Analyses show that shallow convection and cloud microphysics processes explain most of the increased LWP in GFu and GFv compared to MSKFu and MSKFv, and satellite-derived data. We plan to update the GF shallow convection scheme with that implemented in version 4.1 of the Advanced Research Weather Forecast (WRF) model. Because the updated scheme includes an improved cloud model that allows water vapor and cloud liquid water to detrain separately and a fraction of condensed water to precipitate, we will focus on the impact of explicit detrainment of cloud liquid water and precipitation from shallow convective updrafts on the simulated LWP in GF. Results show that MSKF underestimates shallow convection, leading the troposphere below 700 hPa to be drier than actually observed. These results imply that the shallow convection in MSKF needs to be updated or that a separate parameterization of shallow convection needs to be used in addition to that in MSKF. Using the same parameterization of shallow convection, and partitioning of the detrained condensed water between cloud liquid water and ice in GF and MSKF, will further provide understanding in the partitioning of the LWP between subgrid-scale deep and shallow convection. Variable-resolution experiments strongly overestimate the IWP compared to CERES-SSF data over the refined area of the mesh, leading to strong biases in the cloud fraction, and TOA long- and short-wave radiation. Because subgrid-scale deep convection is reduced at increased horizontal resolutions, grid-scale cloud microphysics contributes a major part to biases in the simulated IWP.

Parameterizing the dependence of subgrid-scale deep convection as a function of horizontal resolution allows the use of variable-resolution meshes spanning between hydrostatic and nonhydrostatic scales within a global framework

798   for regional NWP and climate experiments. Although deep convection is not fully explicitly resolved over the refined

799   area of the mesh in our variables-resolution experiments, it is substantially reduced relative to that over the coarse area

800   of the mesh, allowing to contrast the contribution of subgrid-scale convection and cloud microphysics processes. As

801   horizontal resolution increases from the coarse to refined area of the mesh, deep convection gradually transitions from

802   parameterized to resolved and cloud microphysics contribute a major part to moist processes over the refined mesh.

803   Shallow convection coupled with grid-scale microphysics contributes a major part to the low-level cloud liquid water

804   and mixed-phase clouds whereas grid-scale cloud microphysics contribute a major part to the formation of upper-

805   tropospheric ice clouds over the refined area. Our results show that mesh refinement does not systematically improve

806   precipitation and clouds over the Tropical Pacific Ocean as grid-scale condensation increases at increased resolutions.

807   As cloud microphysics processes drive the moisture budget over the refined area of the mesh, we propose to expand

808   this diagnostic study to a process study by further understanding the cloud microphysics processes that need to be

809   improved in order to reduce discrepancies between model and observations. In that vein, the recently developed MSKF

810   that includes a double moment microphysics (Glotfelty et al., 2019) would be useful in a future process study.

811

812

813   *Code and data availability*: The source code used to initialize and run our experiments is based on MPAS-v5.2 which

814   is freely available from https://github.com/MPAS-Dev/MPAS-Model/releases/tag/v5.2. Modifications to the original

815   source code and scripts to run the experiments are available from https://doi.org/10.5281/zenodo.3515440 (Fowler,

816   2019) while initialization files, and outputs from the experiments are located on the NCAR Campaign Storage System.

817   These files can be made available by contacting the corresponding author. Examples of CERES SSF Aqua and Terra

818   orbital and gridded data, daily-mean and monthly-mean simulated diagnostics, and post-processing scripts are also

819   available from https://doi.org/10.5281/zenodo.3515440 (Fowler, 2019).

820

821

822   *Author contributions*: LF developed all the modifications that were made to the MPAS-v5.2 released version and were

823   necessary to run the different experiments. KA made all the updates to the MultiScale Kain-Fritsch parameterization

824   of convection. LF and MB designed the experiments, and LF conducted and analyzed the simulations. LF prepared

825   the manuscript with contributions from all co-authors.

826

827

828   *Competing interests*: The authors declare that they have no conflict of interest.

829

830

831   *Acknowledgments:* This research is based upon work supported by the National Center for Atmospheric Research

832   which is a major facility sponsored by the National Science Foundation under Cooperative Agreement No. 1852977.

833   The authors thank Dr. Hugh Morrison for his careful review and constructive suggestions of the manuscript prior to

834   its submission. The authors thank two anonymous reviewers for their valuable comments and critics that helped

835 improve the clarity of the manuscript. The CERES-SSF data were obtained from the NASA Langley Research Center
836 Atmospheric Science Data Center. The TMPA data were acquired as part of the activities of NASA's Science Mission
837 Directorate and are archived and distributed by the Goddard Earth Sciences (GES) Data and Information Services
838 Center (DISC). We would like to acknowledge high-performance computing support from Cheyenne
839 (doi:10.5065/D6RX99hX) provided by NCAR's Computational and Information Systems Laboratory, sponsored by
840 the National Science Foundation. We acknowledge the use of the NCAR Command Language (Version 6.3.2)
841 [Software]. (2019). Boulder, Colorado: UCAR/NCAR/CISL/TDD. http://dx.doi.org/10.5065/D6WD3XH5 for all
842 figures.

843 **References**

844 Alapaty, K., Herwehe, J.A., Otte, T.L., Nolte, C.G., Bullock, O.R., Ballard, M.S., Kain, J.S., and Dudhia, J.:
845   Introducing subgrid-scale cloud feedbacks to radiation for regional meteorological and climate modeling,
846   Geophys. Res. Lett., 39, L24809, https://doi.org/10.1029/2012GL054031, 2012.

847 Alishouse, J.C., Snider, J.B., Westwater, E.R., Swift, C.T., Ruf, C.S., Vongsathron, S.A., and Ferraro, R.R.:
848   Determination of cloud liquid water content using the SSM/I, IEEE T. Geosci. Remote, 28, 817-822,
849   https://doi.org/10.1109/36.58968, 1990.

850 Arakawa, A., and Schubert, W.H.: Interaction of a cumulus cloud ensemble with the large-scale environment, Part I,
851   J. Atmos. Sci., 31, 674-701, https://doi.org/10.1175/1520-0469(1974)031<0674:IOACCE>2.0.CO;2, 1974.

852 Arakawa, A., and Wu, C.-M.: A unified representation of deep moist convection in numerical modeling of the
853   atmosphere. Part I, J. Atmos. Sci., 70, 1977-1992, https://doi.org/10.1175/JAS-D-12-0330.1, 2013.

854 Bechtold, P., Bazile, E., Guichard, F., Mascart, P., and Richard, E.: A mass-flux convection scheme for regional and
855   global models, Q. J. Roy. Meteor. Soc., 130, 3139-3172, https://doi.org/10.1002/qj.49712757309, 2001.

856 Bechtold, P., Köhler, M., Jung, T., Doblas-Reyes, F., Leutbecher, M., Rodwell, M. J., Vitart, F., and Balsamo, G.:
857   Advances in simulating atmospheric variability with the ECMWF model: From synoptic to decadal time-scales,
858   Q. J. Roy. Meteor. Soc., 134, 1337–1351, https://doi.org/10.1002/qj.289, 2008.

859 Brown, J.M.: Mesoscale unsaturated downdrafts driven by rainfall evaporation: A numerical study, J. Atmos. Sci., 36,
860   313-338, https://doi.org/10.1175/1520-0469(1979)036<0313:MUDDBR>2.0.CO;2, 1979.

861 Chen, F., and Dudhia, J.: Coupling an advanced land surface-hydrology model with the Penn State-NCAR MM5
862   modeling system. Part I: Model implementation and sensitivity, Mon. Weather Rev., 129, 569-585,
863   https://doi.org/10.1175/1520-0493(2001)129<0569:CAALSH>2.0.CO;2, 2001.

864 Dee, D.P., and 35 co-authors: The ERA-Interim reanalysis: configuration and performance of the data assimilation
865   system, Q. J. Roy. Meteor. Soc., 137, 553-597, https://doi.org/10.1002/qj.828, 2011.

866 Dolinar, E.K., Dong, X., Xi, B., Jiang, J.H., and Su, H.: Evaluation of CMIP5 simulated clouds and TOA radiation
867   budgets using NASA satellite observations, Clim. Dynam., 44, 2229-2247, https://doi.org/10.1007/s00382-014-
868   2158-9, 2015.

869 Fowler, L.D., Skamarock, W.C., Grell, G.A., Freitas, S.R., and Duda, M.G.: Analyzing the Grell-Freitas convection
870   scheme from hydrostatic to nonhydrostatic scales within a global model, Mon. Weather Rev., 144, 2285-2306,
871   https://doi.org/10.1175/MWR-D-15-0311.1, 2016.

872 Frank, W.M., and Cohen, C.: Simulation of tropical convective systems. Part I: A cumulus parameterization, J. Atmos.
873   Sci., 44, 3787-3799, https://doi.org/10.1175/1520-0469(1987)044<3787:SOTCSP>2.0.CO;2, 1987.

874 Fritsch, J.M., and Chappell, C.F.: Numerical prediction of convectively driven mesoscale pressure systems. Part I:
875   Convective parameterization, J. Atmos. Sci., 37, 1722–1733, https://doi.org/10.1175/1520-
876   0469(1980)037<1722:NPOCDM>2.0.CO;2, 1980.

877 Fowler, L.D.: experimentsMPAS-v5.2, Zenodo, https://doi.org/10.5281/zenodo.3515440, 2019.

878 Geier, E.B., Green, R.N., Kratz, D.P., Minnis, P., Miller, W.F., Nolan, S.K., and Franklin, C.B.: Clouds and the Earth's
879   Radiant Energy System (CERES) data management system. Single Satellite Footprint TOA/Surface Fluxes and
880   Clouds (SSF) collection document. Release 2, Version 1, 243 pp, 2003.

881 Giorgetta, M.A., Brokopf, R., Crueger, T., Esch, M., Fiedler, S., Helmert, J., Hohenegger, C., Kornblueh, L., Köhler,
882   M., Manzini, E., Mauritsen, T., Nam, C., Raddatz, T., Rast, S., Reinert, D., Sakradzija, M., Schmidt, H., Schneck,
883   R., Schnur, R., Silvers, L., Wan, H., Zängl, G., and Stevens, B: ICON-A, the atmosphere component of the ICON
884   Earth System Model: I. Model description, J. Adv. Model. Earth Sy.10, 1613-1637,
885   https://doi.org/10.1029/2017MS001242, 2018.

886 Glotfelty, T., Alapaty, K., He, J., Hawbecker, P., Song, X., and Zhang, G.: The Weather Research and Forecasting
887   Model with aerosol cloud-interactions (WRF-ACI): Development, evaluation, and initial applications, Mon. Wea.
888   Rev., 147, 1491-1511, https://doi.org/10.1175/MWR-D-18-0267.1, 2019.

889 Greenwald, T.J., Stephens, G.L., Vonder Haar, T.H., and Jackson, D.L.: A physical retrieval of cloud liquid water
890   over global oceans using special sensor microwave/imager (SSM/I) observations, J. Geophys. Res., 98, 18471-
891   18488, https://doi.org/10.1029/93JD00339, 1993.

892 Grell, G.A.: Prognostic evaluation of assumptions uses by cumulus parameterizations, Mon. Weather Rev., 121, 764-
893   787, https://doi.org/10.1175/1520-0493(1993)121<0764:PEOAUB>2.0.CO;2, 1993.

894 Grell, G.A., and Dévényi, D.: A generalized approach to parameterizing convection combining ensemble and data
895   assimilation techniques, Geophys. Res. Lett., 29, 38-1-38-4, https://doi.org/10.1029/2002GL015311, 2002.

896 Grell, G.A., and Freitas, S.R.: A scale and aerosol aware stochastic parameterization for weather and air quality
897   modeling, Atmos. Chem. Phys., 14, 5233-5250, https://doi.org/10.5194/acp-14-5233-2014, 2014.

898 Guo, H., Golaz, J.-C., Donner, L., Wyman, B., Zhao, M., and Ginoux, P.: CLUBB as a unified cloud parameterization:
899   opportunities and challenges, Geophys. Res. Lett., 42, 4540-4547, https://doi.org/10.1002/2015GL063672, 2015.

900 Hagos, S., Leung, L.R., Rauscher, S.A., and Ringler, T.: Error characteristics of two grid refinement approaches in
901   aquaplanet simulations: MPAS-A and WRF, Mon. Wea. Rev., 141, 3022-3036, https://doi.org/10.1175/MWR-
902   D-12-00338.1, 2013.

903 He, J., and Alapaty, K.: Precipitation partitioning in multiscale atmospheric simulations: Impacts of stability
904   restoration methods, J. Geophys. Res., 123, 10185-10201, https://doi.org/10.1029/2018JD028710, 2018.

905 Herwehe, J.A., Alapaty, K., and Bullock Jr., O.R: Evaluation of developments toward a multi-scale Kain-Fritsch
906   parameterization in WRF. 2014 Community Modeling and Analysis System Conference, Chapel Hill, NC, EPA,
907   2014.

908 Hong, S.-Y., and Lim, J.-O: The WRF single moment 6-class microphysics scheme (WSM6), J. Korean Meteor. Soc.,
909   42, 129-151, 2006.

910 Hong, S.-Y., Choi, J., Chang, E.-C., Park, H., and Kim Y.-J.: Lower-tropospheric enhancement of gravity wave drag
911   in a global spectral atmospheric forecast model, Weather Forecast, 23, 523-531,
912   https://doi.org/10.1175/2007WAF2007030.1, 2008.

913 Huffman, G.J., Balvin, D.T., Nelkin, E.J., and Wolff, D.B.: The TRMM Multisatellite Precipitation Analysis (TMPA):
914   Quasi-global, multiyear, combined-sensor precipitation at fine scales, J. Hydrometeorol., 8, 38-55,
915   https://doi.org/10.1175/JHM560.1, 2007.

916 Iacono, M. J., Mlawer, E. J., Clough, S. A., and Morcrette, J.-J.: Impact of an improved longwave radiation model,
917   RRTM, on the energy budget and thermodynamic properties of the NCAR Community Climate Model, CCM3,
918   J. Geophys. Res., 105, 14 873–14 890, https://doi.org/10.1029/2000JD900091, 2000.

919 Jiang, J.H., Su, H., Zhai, C., Perun, V.S, Del Genio, A., Nazarenko, L.S., Donner, L.J., Horowitz, L., Seman, C., Cole,
920   J., Gettelman, A., Ringer, M.A., Rotstayn, L., Jeffrey, S., Wu, T., Brient, F., Dufresne, J.-L., Kawai, H., Koshiro,
921   T., Watanabe, M., L'Ecuyer, T.S., Volodin, E.M., Iversen, T., Drange, H., Mesquita, M.D.S., Read, W.G., Waters,
922   J.W., Tian, B., Teixeira, J., and Stephens, G.L.: Evaluation of cloud and water vapor simulations in CMIP5
923   climate models using NASA "A-Train" satellite observations, J. Geophys. Res., 117, D14105,
924   https://doi.org/10.1029/2011JD017237, 2012.

925 Ju, L., Ringler, T., and Gunzburger, M.: Voronoi tessellations and their applications to climate and global modeling,
926   Numerical Techniques for Global Atmospheric Models, P. Lauritzen et al., Eds., Springer, 313-342, 2011.

927 Judt, F.: Atmospheric predictability of the tropics, middle latitudes, and polar regions explored through global storm-
928   resolving simulations, J. Atmos. Sci., 77, 257-276, https://doi.org/: 10.1175/JAS-D-19-0116.1, 2020.

929 Kain, J.S.: The Kain-Fritsch parameterization: An update, J. Appl. Meteorol., 43, 170-181,
930   https://doi.org/10.1175/1520-0450(2004)043<0170:TKCPAU>2.0.CO;2, 2004.

931 Kain, J.S, and Fritsch, J.M.: A one-dimensional entraining/detraining plume model and its application in convective
932   parameterization, J. Atmos. Sci., 47, 2784-2802, https://doi.org/10.1175/1520-
933   0469(1990)047<2784:AODEPM>2.0.CO;2, 1990.

934 Kain, J.S., and Fritsch, J.M.: The role of convective "trigger function" in numerical forecasts of mesoscale convective
935   systems, Meteorol. Atmos. Phys., 49, 93-106, https://doi.org/10.1007/BF01025402, 1992.

936 Kain, J.S., and Fritsch, J.M.: Convective parameterization for mesoscale models: The Kain-Fritsch scheme, The
937   Representation of Cumulus Convection in Numerical Models, Meteor. Mon., No. 24, American Meteorological
938   Society, Boston, MA, 165-170, https://doi.org/10.1007/978-1-935704-13-3_16, 1993.

Kay, J.E., Deser, C., Phillips, A., Mai, A., Hannary, C., Strand, G., Arblaster, J.M., Bates, S.C., Danabasoglu, G., Edwards, J., Holland, M., Kushner, P., Lamarque, J.-F., Lawrence, D., Lindsay, K., Middleton, A., Munoz, E., Neale, R., Oleson, K., Polvani, L., and Vertenstein, M.: The Community Earth System Model (CESM) large ensemble project, B. Am. Meteorol. Soc., 96, 1333-1349, https://doi.org/10.1175/BAMS-D-13-00255.1, 2015.

Kessler, E.: On the distribution and continuity of water substances in atmospheric circulation, Meteor. Mon., No. 10, American Meteorological Society, Boston, MA, 1-84, https://doi.org/10.1007/978-1-935704-36-2_1, 1969.

Klemp, J.B.: A terrain-following coordinate with smoothed coordinate surfaces, Mon. Weather Rev., 139, 2163-2169, https://doi.org/10.1175/MWR-D-10-05046.1, 2011

Klemp, J.B., Skamarock, W.C., and Dudhia, J.: Conservative split-explicit time integration methods for the compressible nonhydrostatic equations, Mon. Weather Rev., 135, 2897-2913, https://doi.org/10.1175/MWR3440.1, 2007.

Krishnamurti, T.N., Low-Nam, S., and Pasch, R.: Cumulus parameterization and rainfall rates II, Mon. Weather Rev., 111, 815-828, https://doi.org/10.1175/1520-0493(1983)111<0815:CPARRI>2.0.CO;2, 1983.

Li, J.-L., Waliser, D., Woods, C., Teixeira, J., Bacmeister, J., Chern, J., Shen, B.-W., Tompkins, A., Tao, W.-K., and Köhler, M.: Comparisons of satellites liquid water estimates to ECMWF and GMAO analyses, 20th century IPCC AR4 climate simulations and GCM simulations, Geophys. Res. Lett., 35, L9710, https://doi.org/10.1029/2008GL035427, 2008.

Li, J.-L., Waliser, D.E., Chen, W.-T., Guan, B., Kubar, T., Stephens, G., Ma, H.-Y., Deng, M., Donner, L., Seman, C., and Horowitz, L.: An observational based evaluation of cloud ice water in CMIP3 and CMIP5 GCMs and contemporary reanalyses using contemporary satellite data, J. Geophys. Res., 117, D16105, https://doi.org/10.1029/2012JD017640, 2012.

Li, J.-L., Lee, S., Ma, H.-Y, Stephens, G., and Guan, B.: Assessment of the cloud liquid water from climate models and reanalysis using satellite observations, Terr. Atmos. Ocean. Sci., 29(6), 653-678, https://doi.org/10.3319/TAO.2018.07.04.01, 2018.

Mahoney, K.M.: The representation of cumulus convection in high-resolution simulations of the 2013 Colorado front range flood, Mon. Weather Rev., 144, 4265-4278, https://doi.org/10.1175/MWR-D-16-0211.1, 2016.

Meehl, G.A., Delworth, T.L., Latiff, M., McAveney, B., Mitchell, J.F.B., Stouffer, R.J., and Taylor. K.E.: The WCRP CMIP3 multimodel dataset: A new era in climate change research, B. Am. Meteorol. Soc., 88, 1383-1394, https://doi.org/10.1175/BAMS-88-9-1383, 2007.

Minnis, P., and coauthors: CERES Edition-2 cloud property retrievals using TRMM VIRS and Terra and Aqua MODIS data-Part I: Algorithms, IEEE T. Geosci. Remote., Vol. 49, NO 11, 4374-4400, https://doi.org/10.1109/TGRS.2011.2144601, 2011.

Minnis, P., Kratz, D.P, Coakley, J.J.A., King, M.D., Garber, D., Heck, P., Mayor, S., Young, D.F., and Arduini, R.: Cloud optical property retrieval (Subsystem 4.3), in Clouds and the Earth's Radiant Energy System (CERES)

Algorithm Theoretical Basis Document, Vol III, Clouds and Radiance Inversions (Subsystem 4), NASA RP 1376, edited by Science Team CERES, pp. 135-176, NASA, Washington D.C., 1995.

Mlawer, E. J., Taubman, S. J., Brown, P. D., Iacono, M. J., and Clough, S. A.: Radiative transfer for inhomogeneous atmospheres: RRTM, a validated correlated-k model for the longwave, J. Geophys. Res., 102, 16663–16682, https://doi.org/10.1029/97JD00237, 1997.

Molod, A., Takacs, L., Suarez, M., Bacmeister, J., Song, I.-S., and Eichman, A.: The GEOS-5 atmospheric general circulation model: Mean climate from MERRA to Fortuna, Technical Report Series on Global Modeling and Assimilations, Vol. 28, 124 pp, 2012.

Moorthi, S., and Suarez, M.J.: Relaxed Arakawa-Schubert: a parameterization of moist convection for general circulation models, Mon. Wea. Rev., 210, 978-1002, https://doi.org/10.1175/1520-0493(1992)120<0978:RASAPO>2.0.CO;2, 1992.

Nakanishi, M., and Niino, H.: Development of an improved turbulence closure model for the atmospheric boundary layer, J. Meteor. Soc. Japan, 87, 895–912, https://doi.org/10.2151/jmsj.87.895, 2009.

Ogura, Y., and Cho, H.-R.: Diagnostic determination of cumulus cloud populations from observed large-scale variables, J. Atmos. Sci., 30, 1276-1286, https://doi.org/10.1175/1520-0469(1973)030<1276:DDOCCP>2.0.CO;2, 1973.

Olson, J.B., Kenyon, J.S., Angevine, W.M., Brown, J.M., Pagowski, M., and Suselj, K.: A description of the MYNN-EDMF scheme and the coupling to other components in WRF-ARW, NOAA Technical Memorandum OAR GSD, 61, pp 37, 2019.

Platnick, S., King, M.D., Ackerman, S.A., Wenzel, W.P., Baum, B.A., Riedl, J.C., and Frey, R.A.: The MODIS cloud products: Algorithms and examples from Terra, IEEE T. Geosci. Remote, 41, 459-473, https://doi.org/10.1109/TGRS.2002.808301, 2003.

Qiao, F., and Liang, X-Z: Effects of cumulus parameterization closures on the simulations of summer precipitation over the United States coastal oceans, J. Adv. Model. Earth Sy., 8, 764-785, https://doi.org/10.1002/2015MS000621, 2015.

Raymond, D.J.: Regulation of moist convection over the west Pacific warm pool, J. Atmos. Sci., 52, 3945-3959, https://doi.org/10.1175/1520-0469(1995)052<3945:ROMCOT>2.0.CO;2, 1995.

Sakaguchi, K., Leung, L.R., Zhao, C., Yang, Q., Lu, J., and Hagos, S.: Exploring a multiresolution approach using AMIP simulations, J. Clim., 28, 5549-5574, https://doi.org/ 10.1175/JCLI-D-14-00729.1, 2015.

Schwarz, C.S.: Medium-range convection-allowing ensemble forecasts with a variable-resolution global model, Mon. Weather Rev., 147, 2997-3023, https://doi.org/10.1175/MWR-D-18-0452.1, 2019.

Simpson, J., and Wiggert, V.: Models of precipitating cumulus towers, Mon. Weather Rev., 97, 471-489, https://doi.org/10.1175/1520-0493(1969)097<0471:MOPCT>2.3.CO;2, 1969.

1006   Skamarock, W.C., and Gassmann, A.: Conservative transport schemes for spherical geodesic grids: High-order flux
1007   operators for ODE-based time integration, Mon. Weather Rev., 139, 2962-2975, https://doi.org/10.1175/MWR-
1008   D-10-05056.1, 2011.

1009   Skamarock, W.C., Klemp, J.B., Duda, M.G., Fowler, L.D., Park, S.-H., and Ringler, T.D.: A multiscale nonhydrostatic
1010   atmospheric model using Centroidal Voronoi tessellations and C-grid staggering, Mon. Weather Rev., 140, 3090-
1011   3105, https://doi.org/10.1175/MWR-D-11-00215.1, 2012.

1012   Skamarock, W.C., and Coauthors: A description of the Advanced Research WRF version 3, NCAR Tech. Note
1013   NCAR/TN-475+STR, 113 pp, 2008.

1014   Smagorinsky, J.: General circulation experiments with the primitive equations. I. The basic experiment, Mon. Weather
1015   Rev., 91, 99-164, https://doi.org/10.1175/1520-0493(1963)091<0099:GCEWTP>2.3.CO;2, 1963.

1016   Stanfield, R.E., Dong, X., Xi, B., Del Genio, A.D., Minnis, P., Doelling, D., and Loeb, N.: Assessment of NASA
1017   GISS CMIP5 and Post-CMIP5 simulated clouds and TOA radiation budgets using satellite observations. Part II:
1018   TOA radiation budget and CREs, J. Climate, 28, 1842-1863, https://doi.org/10.1175/JCLI-D-14-00249.1, 2015.

1019   Stephens, G.L., and Kummerow, C.D.: The remote sensing of clouds and precipitation from space: A review, J. Atmos.
1020   Sci., 64, 3742-3765, https://doi.org/10.1175/2006JAS2375.1, 2007.

1021   Stephens, G.L., Vane, D.G., Boain, R.J., Mace, G.G., Sassen, K., Wang, Z., Illingworth, A.J., O'Connor, E.J., Rossow,
1022   W.B., Durden, S.L., Miller, S.D., Austin, R.T., Benedetti, A., Mitrescu, C., and the CloudSat Science Team: The
1023   CloudSat mission and the A-Train: A new dimension and space-based observations of clouds and precipitation,
1024   B. Am. Meteorol. Soc., 83, 1771-1790, https://doi.org/10.1175/BAMS-83-12-1771, 2002.

1025   Storer, R.L., Griffin, B.M., Hoft, J., Weber, J.K., Raut, E., Larson, V.E., Wang, M., and Rasch, P.J.: Parameterizing
1026   deep convection using the assumed probability density function method, Geosci. Model Dev., 8, 1-19,
1027   https://doi.org/10.5194/gmd-8-1-2015, 2015.

1028   Strauss, D., and Paolino, D.: Intermediate time error growth and predictability: tropics versus mid-latitudes, Tellus A:
1029   Dynamics and Meteorology and Oceanography, 61, 579-586, https://doi.org/10.1111/j.1600-0870.2009.00411.x,
1030   2008.

1031   Suhas, E., and Zhang, Q.J.: Evaluation of trigger functions for convective parameterization schemes using
1032   observations, J. Climate, 27, 7647-7666, https://doi.org/10.1175/JCLI-D-13-00718.1, 2014.

1033   Taylor, K.E., Stouffer, R.J., and Meehl, G.A.: An overview of CMIP5 and the experiment design, B. Am. Meteorol.
1034   Soc., 93, 485-4398, https://doi.org/10.1175/BAMS-D-11-00094.1, 2012.

1035   Thayer-Calder, K., Gettelman, A., Craig, C., Goldhaber, S., Bogenschutz, P.A., Chen, C.-C., Morrison, H., Höft, J.,
1036   Raut, E., Griffin, B.M., Weber, J.K., Larson, V.E., Wyant, M.C., M. Wang, Guo, Z., and Ghan, S.J.: A unified
1037   parameterization of clouds and turbulence using CLUBB and subcolumns in the Community Atmosphere Model,
1038   Geosic. Model Dev., 8, 3801-3821, https://doi.org/10.5194/gmd-8-3801-2015, 2015.

1039   Thompson, G., Field, P.R., Rasmussen, R.M., and Hall, W.D.: Explicit forecasts of winter precipitation using an
1040   improved bulk cloud microphysics scheme. Part II: Implementation of a new snow parameterization, Mon.
1041   Weather Rev., 136, 5095-5115, https://doi.org/10.1175/2008MWR2387.1, 2008.

1042   Thompson, G., Rasmussen, R.M., and Manning, K.: Explicit forecasts of winter precipitation using an improved bulk
1043   cloud microphysics scheme. Part I: Description and sensitivity analysis, Mon. Weather Rev., 132, 519-542,
1044   https://doi.org/10.1175/1520-0493(2004)132<0519:EFOWPU>2.0.CO;2, 2004.

1045   Thompson, G., Tewari, M., Ikeda, K., Tessendorf, S., Weeks, C., Otkin, J., and Kong, F.: Explicitly-coupled cloud
1046   physics and radiation parameterizations and subsequent evaluation in WRF high-resolution convective forecasts,
1047   Atmos. Res., 168, 92-104, https://doi.org/10.1016/j.atmosres.2015.09.005, 2016.

1048   Tokioka, T., Yamazaki, K., Kotoh, A., and Ose, T.: The equatorial 30-60 day oscillation and the Arakawa–Schubert
1049   penetrative cumulus parameterization, J. Meteor. Soc. Japan, 66, 883–900,
1050   https://doi.org/10.2151/jmsj1965.66.6_883, 1988.

1051   Waliser, D.E., Li, J.-L., Woods, C.P., Austin, R.T., Bacmeister, J., Chern, J., Del Genio, A., Jiang, J.H., Juang, Z.,
1052   Meng, H., Minnis, P., Platnick, S., Rossow, W.B., Stephens, G.L., Sun-Mack, S., Tao, W.-K., Tompkins, A.M.,
1053   Vane, D.G., Walker, C., and Wu, D.: Cloud ice: A climate model challenge with signs and expectations of
1054   progress, J. Geophys. Res., 114, D00A21, https://doi.org/10.1029/2008JD010015, 2009.

1055   Wicker, L.J., and W.C. Skamarock: Time-splitting methods for elastic models using forward time schemes, Mon.
1056   Weather Rev., 130, 2088-2097, https://doi.org/10.1175/1520-0493(2002)130<2088:TSMFEM>2.0.CO;2, 2002.

1057   Wielicki, B.A., Barkstrom, B.R., Harrison, E.F., Lee III, R.B., Smith, G.L., and Cooper, J.E.: Clouds and the Earth's
1058   Radiation Energy System (CERES): An Earth Observing System experiment, B. Am. Meteorol. Soc., 77, 853-
1059   868, https://doi.org/10.1175/1520-0477(1996)077<0853:CATERE>2.0.CO;2, 1996.

1060   Williamson, D.: The effect of time step and time-scales on parameterization suites. Quart. J. Roy. Meteor. Soc., 139,
1061   548-560, https://doi.org/10.1002/qj.1992, 2013.

1062   Wong, M., and Skamarock, W.C.: Spectral characteristics of convective-scale precipitation observations and forecasts,
1063   Mon. Weather Rev., 144, 4183-4195, https://doi.org/10.1175/MWR-D-16-0183.1, 2016.

1064   Xu, K.-M. and Krueger, S.K.: Evaluation of cloudiness parameterizations using a cumulus ensemble model, Mon.
1065   Weather Rev., 119, 342-367, https://doi.org/10.1175/1520-0493(1991)119<0342:EOCPUA>2.0.CO;2, 1991.

1066   Xu, K.-M., and Randall, D. A.: A semi-empirical cloudiness parameterization for use in climate models, J. Atmos.
1067   Sci., 53, 3084–3102, https://doi.org/10.1175/1520-0469(1996)053<3084:ASCPFU>2.0.CO;2, 1996.

1068   Zheng, Y., Alapaty, K., Herwehe, J. A., Del Genio, A.D., and Niyogi, D.: Improving high-resolution weather forecasts
1069   using the Weather Research and Forecasting (WRF) model with an updated Kain-Fritsch scheme, Mon. Weather
1070   Rev., 144, 833-860, https://doi.org/10.1175/MWR-D-15-0005.1, 2016.